Chemical Geology 581 (2021) 120403

Contents lists available at ScienceDirect

Chemical Geology

journal homepage: www.elsevier.com/locate/chemgeo

The role of microbial extracellular polymeric substances on formation of sulfate minerals and fibrous Mg-clays

Pablo del Buey [a,*], M. Esther Sanz-Montero [a,**], Olivier Braissant [b], Óscar Cabestrero [a], Pieter T. Visscher [c,d]

[a] Department of Mineralogy and Petrology, Univ. Complutense Madrid, 28040 Madrid, Spain
[b] Department of Biomedical Engineering, Univ. Basel, 4123 Allschwil, Switzerland
[c] Departments of Marine Sciences and Geosciences, Univ. Connecticut, 06340 Groton, USA
[d] UBFC Biogeosciences, Dijon, France

ARTICLE INFO

Editor: Hailiang Dong

Keywords:
Exopolymer
Intrasedimentary precipitation
Sulfate
Mg-silicate
EPS desiccation
Hypersaline mat

ABSTRACT

A variety of Mg-, Na- and Ca-sulfates, including gypsum, and Mg-clays precipitate within the microbial mats that developed seasonally in the hypersaline playa lake El Longar (Central Spain). A multidisciplinary study of the microbial mats along a transect of the lake demonstrates that the degree of lithification of the mats increases from the soft and poorly lithified layers lying on the submerged ground to the highly crystalline mats present in the desiccated fringes.

The community composition of the mats is diverse, dominated in terms of OTUs by *Proteobacteria*, *Firmicutes* and *Cyanobacteria*. The *Proteobacteria* include sulfur-cycling microbes, supporting biogeochemical cycling of this element. *Cyanobacteria* are the dominant EPS producers in microbial mats and *Firmicutes* and *Proteobacteria* have both been shown to play a role in EPS turnover.

Several ions (e.g., Mg, S, Si, Al, Fe, Ca, Na) are bound to functional groups of EPS. The abundance of sulfate groups and carboxylic acids suggested that the EPS have a strong binding capacity for Mg^{2+} and Ca^{2+}, which were higher in the submerged microbial mats. Na, Mg, K, Ca, SO_4^{2-} and Si are more concentrated in the EPS matrices than in the natural brines. The concentration of ions in the EPS is sufficient to precipitate a mixture of minerals through freeze-drying, that is similar to that found in intact mats. In the EPS of the submerged mats precipitate more types of minerals, including sulfates and Mg-clays, than in the EPS of the exposed areas. These results suggest that the mineral nucleation occurred during the degradation of the mats when the EPS was progressively desiccated and likely released high amounts of ions.

The present study helps to understand intrasedimentary growth of sulfates and clays in microbial mats. The presence of these mineral assemblage can be related to a potential biosignature of microbial past life on Earth and possibly also on exoplanets, like Mars.

1. Introduction

Microbial mats are laminated organosedimentary benthic microbial communities that trap and bind detrital sediment or induce mineral precipitation (Burne and Moore, 1987). These mats constitute ecosystems made up of primary producers and decomposers (Van Gemerden, 1993; Visscher and Stolz, 2005). Microbial mats are found in a wide variety of environments, including fossil lacustrine environments (Sanz-Montero et al., 2008; Awramik and Buchheim, 2009) and their modern counterparts (Van Gemerden, 1993; Des Marais, 1995).

Hypersaline lakes are quintessential environments for microbial mats to develop (Des Marais, 1995; Dupraz et al., 2004; Cabestrero et al., 2018a). Seasonal fluctuations in ion concentrations typical for the hypersaline and ephemeral lakes support the development of microbial mats (Stal et al., 1984; Visscher and Stolz, 2005; Dupraz et al., 2004; Braissant et al., 2007; Sanz-Montero and Rodríguez-Aranda, 2013; Sanz-Montero et al., 2013; Sanz-Montero et al., 2015; Cabestrero et al., 2018b). Widespread presence of microbial mats promotes

* Corresponding author.
** Corresponding author.
E-mail addresses: pablodelbuey@ucm.es (P. del Buey), mesanz@ucm.es (M.E. Sanz-Montero).

https://doi.org/10.1016/j.chemgeo.2021.120403
Received 1 March 2021; Received in revised form 17 June 2021; Accepted 21 June 2021
Available online 24 June 2021

hydrogeochemical changes through their metabolic activities and binding capacities (Gerdes et al., 2000) and plays a role in brine evolution (Cabestrero and Sanz-Montero, 2018). Microbial mats could provide a matrix within which hydrated and anhydrous sulfates grow, e.g., forming biolaminites (Rouchy and Monty, 2000; Cabestrero et al., 2018a).

The importance of extracellular polymeric substances (EPS) in mediating the precipitation of carbonate minerals in microbial mats has been widely demonstrated (Visscher et al., 1998; Visscher et al., 2000; Dupraz et al., 2004; Dupraz and Visscher, 2005; Braissant et al., 2007; Pace et al., 2018; Cabestrero and Sanz-Montero, 2018; Sanz-Montero et al., 2019). There is a growing body of evidence showing a that the EPS of microbial mats could provide a matrix within which hydrated and anhydrous sulfates grow, forming biolaminites (Rouchy and Monty, 2000; Sanz-Montero et al., 2013; Cabestrero et al., 2018a). EPS also serve as formation site for clay minerals (Konhauser and Urrutia, 1999; Souza-Egipsy et al., 2005; Bontognali et al., 2014; Burne et al., 2014; Pace et al., 2016; Perri et al., 2017; Del Buey et al., 2018). However, few studies have focused on the role of the microbial EPS matrix on the simultaneous precipitation of sulfate and clay minerals. Many of ancient lacustrine rocks contain good examples of clay minerals associated to intrasedimentary sulfates that crystallized within a host sediment (Calvo et al., 1999), but the origin of such features is uncertain (Spencer, 2001). Host sediments preserved in intrasedimentary evaporites commonly have high organic contents and can preserve biofilms, which may had played a role in mineral precipitation (Sanz-Montero and Rodríguez-Aranda, 2012). Multiple synsedimentary and diagenetic processes can modify the original microbial mat features in ancient saline lakes. Thus, the potential role of the biotic matrices in the intrasedimentary growth of mineral assemblages dominated by sulfates can be better understood through the study of modern microbialites.

The EPS of microbial mats are the product of the interactions between the resident microorganisms and their environment (Decho, 1990). EPS are commonly abundant in microbial mats (Dupraz and Visscher, 2005), especially those present in extreme environments such as hypersaline lakes which desiccate seasonally (Decho and Gutierrez, 2017). Environmental conditions control the production of EPS and determine in part the properties that control their ability to bind metal ions from solution (Dupraz and Visscher, 2005). This capacity of EPS to bind cations results from the pH-dependent deprotonation of functional groups, which increases with pH (Phoenix et al., 2002; Braissant et al., 2007). In addition to proteins, lipids, and nucleic acids, the EPS typically consist of polysaccharides with inorganic functional groups, mostly sulfate and carboxylic acids, but also phosphate and amino groups (Sutherland, 2001; Braissant et al., 2007). Cyanobacteria are presumably the most important EPS producers in microbial mats (Rossi and De Philippis, 2015), but many other organisms also contribute (Decho, 1990; Braissant et al., 2007; Pace et al., 2018). EPS are partially degraded by heterotrophic microorganisms (Visscher et al., 1998; Decho et al., 2005; Braissant et al., 2009; Scheineder et al., 2013). Abiotic alteration of EPS takes place by: UV radiation, photochemically produced super-oxide radicals, changes in ion concentration and temperature (Braissant et al., 2009).

Spain hosts the largest number of ephemeral saline inland lakes in Europe. El Longar (Central Spain) is a permanent mesosaline to hypersaline lake, where most of the sediments are covered with microbial mats. In this lake, the precipitation of sulfates and clay minerals co-occur (Sanz-Montero et al., 2013; Cabestrero and Sanz-Montero, 2018; Cabestrero et al., 2018a; Del Buey et al., 2018). This makes El Longar a perfect natural laboratory to study microbially-induced sulfate- and silicate precipitation.

The aim of this investigation is to analyze the role of the EPS in the simultaneous precipitation of these minerals observed in the microbial mats in the marginal and submerged fringing zones of lake El Longar. The EPS produced by the microbial mat community was studied in order to assess the metal binding capacity of the functional groups in this extracellular organic matrix. This binding capacity determines their potential to precipitate minerals, in El Longar especially that of clays and sulfates. To better understanding the mechanisms of mineral formation, the molecular diversity, mineralogy, hydrochemistry and biogeochemistry of the microbial mats were also studied along a 40 m transect.

2. Materials and methods

2.1. Setting

El Longar (39°42′N 10.26″ W) is a permanent, shallow playa - lake with a surface area of 0.91 km^2, situated 683 masl, with a water depth of up to 0.35 m (Fig. 1). Located in an endorheic wetland in La Mancha region, Central Spain, the lake is positioned on horizontally-bedded Neogene sedimentary rocks consisting of gypsum, chert, carbonates and quartzitic sandstone and conglomerates (Sanz-Montero et al., 2015). The local Mediterranean continental climate is characterized by aridity, with average temperature of 14.3 °C and average annual rainfall of 360 mm and pronounced seasonal and annual fluctuations. The summer months are very dry, which results in the desiccation of the marginal areas of the lake and yields hypersaline conditions (Fig. 1c). El Longar, which is characterized by Mg^{2+}-(Na^{+})-(Ca^{2+})-SO_4^{2-}-(Cl^{-}) brines, accommodates extensive lithifying microbial mats (Sanz-Montero et al., 2013; Cabestrero and Sanz-Montero, 2018; Cabestrero et al., 2018a, 2018b; Del Buey et al., 2018). Precipitation of a wide variety of Ca- Mg- Na sulfates, Mg-clays and carbonates was observed during desiccation (i.e., the late microbial decay stage). The sulfates, which consist of the highly hydrated magnesium and sodium sulfates (epsomite-hexahydrite and mirabilite-thenardite, respectively) and the poorly hydrated minerals, gypsum and polyhalite as well as the double sulfates (bloedite-konyaite and glauberite) commonly precipitate within the microbial mats, often forming extensive biolaminites in the submerged zone of the lake (Cabestrero et al., 2018a).

2.2. Sampling

Sampling was carried out in May 2017 when the lake level had dropped and the shoreline had retreated approximately 40 m horizontally from the highest water level, exposing an emerged shoreline with three (distinctive) fringing microbial mat zones (Fig. 1). The marginal fringing zone was dry, exhibiting a white surface (WFZ) due to subaerial exposure and dehydration of the top of the decaying mats (Fig. 1a). The middle fringing zone (MFZ) retained some water and had a wet surface with a dark grey to black appearance (Fig. 1b). Isolated patches of white precipitates occur on the surface of this zone. Beneath the surface, layering is deeply disrupted by voids filled by fluids, likely produced by degassing of decaying organic material (Figs. 2a–c). The closest to the shoreline, a wide transitional fringing zone (TFZ) in which shallow, interconnected pools developed between crystallized microbial mats (Fig. 1d). Underneath the brine, a fourth partially decayed microbial zone (DSZ) was established (Fig. 1e). Six lithifying microbial mats samples were collected. Among these, four lithifying microbial mat samples were obtained from each zone (Figs. 2a–d). These samples were ca. 1 by 4 cm wide and ca. 3–4 cm deep. One additional microbial mat sample from the TFZ and another mat sample from DSZ were collected for chemical analyses of purified EPS. The microbial mat samples were kept in plastic containers in the dark at 4 °C for up to one week until analysis in the laboratory. Brine samples were collected from the same location as the mat samples and stored in 250 ml sterile polythene bottles at 4 °C. The water samples were filtered in the laboratory using mild vacuum through 0.45 μm pure cellulose acetate membrane filters.

2.3. Hydrochemistry, physicochemical properties and hydrogeochemical modeling

The physicochemical properties of the water column included the

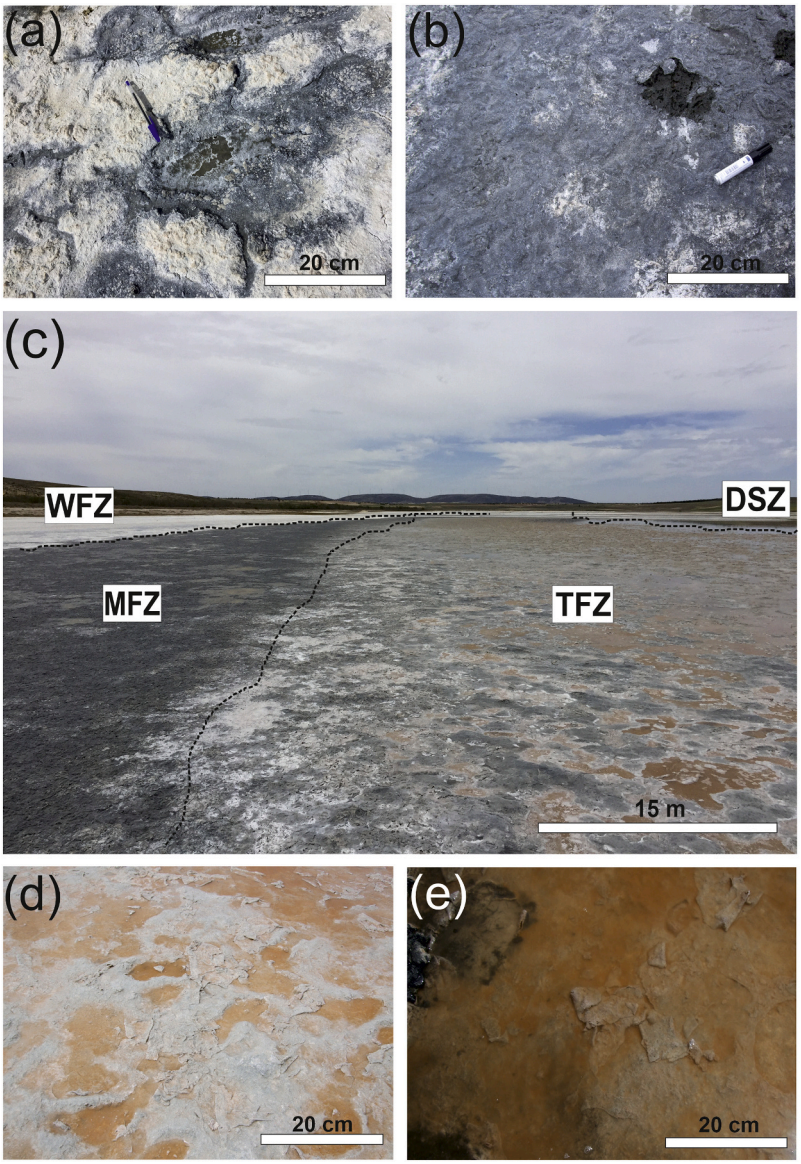

Fig. 1. Overview of the field site showing different fringing zones along El Longar shoreline. (a) Outermost fringe zone (WFZ) showing white mineral precipitates. (b) Middle fringing zone (MFZ) with isolated white patches. (c) Overview of the three exposed to air fringing microbial mat zones of El Longar. (d) Highly lithified microbial mats isolated by brine pools in the transitional fringing zone (TFZ). (e) Poorly lithified microbial mats in the submerged zone of the lake (DSZ).

salinity (S), temperature (T), dissolved oxygen (DO), oxidation-reduction potential (ORP), and pH and were recorded with a portable multiparameter probe (Hanna Instruments 9828). The S value measured by multiparameter probe was unreliable (measurement is not accurate for S˃ 30–40 $g \cdot L^{-1}$), the real value was estimated using dilutions 1:10. Major cations (Ca^{2+}, K^{+}, Mg^{2+}, and Na^{+}) and anions (Br^{-}, Cl^{-}, NO_3^{-}, and SO_4^{2-}) were analyzed in 0.45 μm-filtered water samples by ion chromatography, using a METROHM 940 Professional IC Vario chromatograph. In addition, major cations and Si concentration were analyzed by ICP-AES (SPECTRO Arcos). The carbonate alkalinity (CO_3^{2-} and HCO_3^{-}) of the water was determined by titration.

Hydrogeochemical modeling of overlying water and the two non-purified EPS samples was done using PHREEQC software with the aim of calculating ion activities and saturation indices (SI) for most of the minerals present in the lithifying microbial mat. Due to the high salinity of the lake Pitzer equations were used for the calculation. Brines ionic balance errors were over 5% for both samples (9% and 15%), this makes the saturation indices calculation less reliable. With this assumption made, saturation indices (Table 1) were calculated using ion analytical errors (10%) to obtained a range. PHREEQC cannot calculate with errors, so the range of saturation states was calculated using maximum and minimum concentrations of the ions for each mineral that was considered in each simulation. For instance, maximum saturation index for gypsum of a given water composition was calculated using the maximum value of Ca^{2+} and SO_4^{2-} while the rest of the ions were kept to their concentration minimum (i.e., the ion value minus analytical error in each case). ICP-AES results of the two non-purified EPS samples were also simulated with PHREEQC to assess their potential for mineral precipitation. For this simulation, it is assumed that all ions bound to the EPS are available.

2.4. Petrographic and scanning electron microscopies (FEG-SEM/ESEM)

Optical inspection of one thin section of each of the lithifying microbial mat (Fig. 2a-d and Fig. S3a-g) was performed using petrographic microscopes (Primotech Zeiss and OLYMPUS BX51 equipped with a mercury burner power supply unit). Freshly fracture surfaces of representative samples were air dried and coated with graphite and Au under

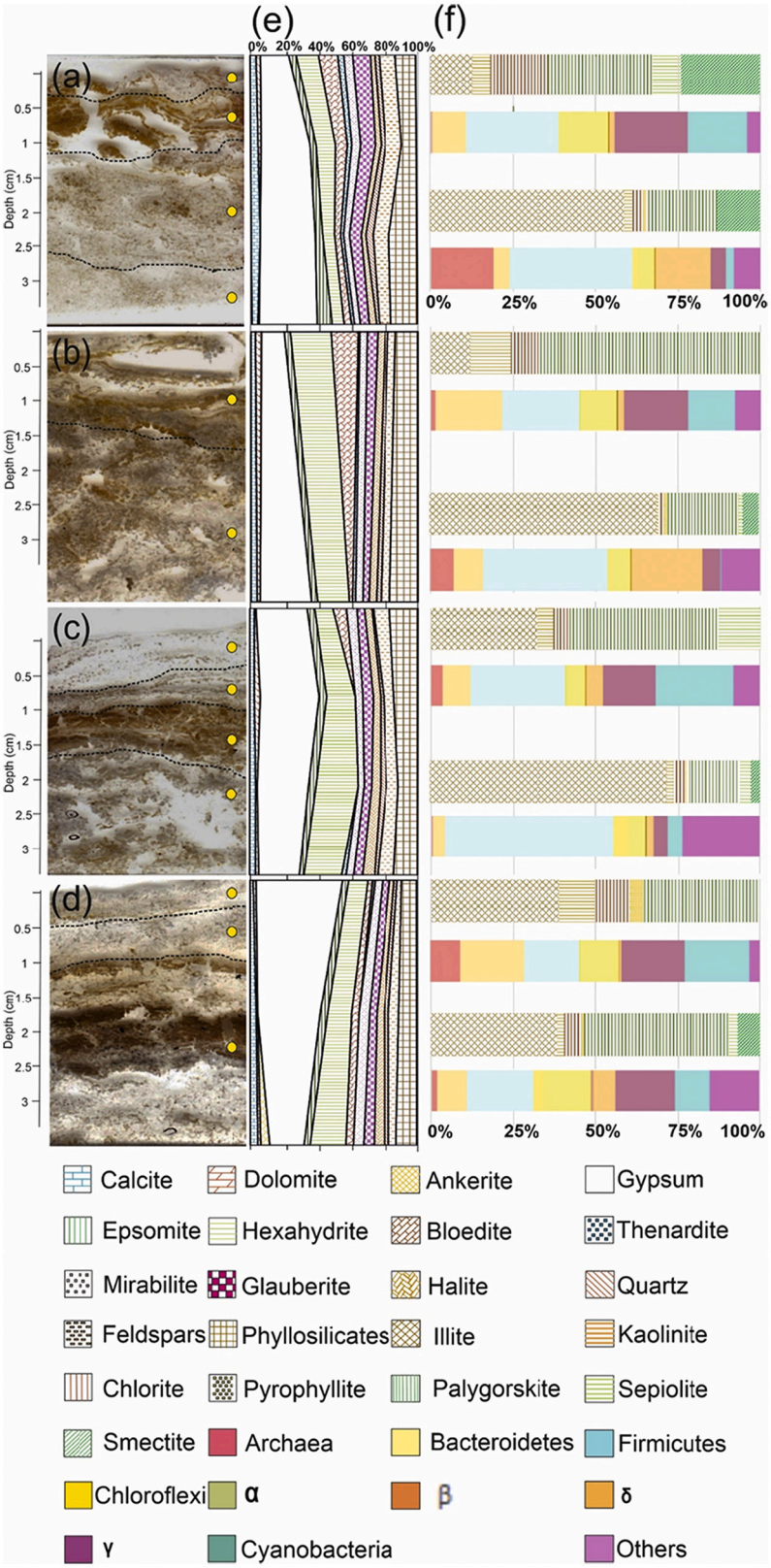

Fig. 2. (a, b, c, d) Petrographic microscopic thin sections images of the upper 3 cm of the lithifying microbial mats, taken along the transect from the margin to the center of the lake (see Fig. 1). Yellow points indicate the individual microbial mats layers sampled for powder XRD analyses. (e) Composition of the bulk mineralogical assemblages in the different layers of the four samples, by weight. (f) Bar graphs showing the clay mineralogy (˂0.5 μm) and the prokaryotic diversity at the phylum and class level two depth horizons.

vacuum conditions. High resolution textural and mineralogical features were observed by scanning electron microscopes (FEI INSPECT ESEM and JEOL JSM 6335F FEG-SEM).

2.5. Bulk and clay mineralogy (XRD)

The mineralogy of the different layers of the four lithifying microbial mats (Fig. 2a-d) along with two non-purified EPS samples (TFZ and DSZ) was examined by powder X-ray diffraction (XRD) analysis using a

Table 1
Physicochemical properties and hydrogeochemical modeling results of the saturation indices of carbonate, sulfate and chloride minerals present in the water overlying the pool (TFZ) and lake water (DSZ) in May 2017. Max, Min and Avg values of the saturation indices represent a range obtained by modeling the ion concentrations ±10% of analytical errors for each mineral.

	TFZ	DSZ
Physicochemical properties		
T (°C)	31.29	30.03
pH	7.17	9.14
ORP	−3.9	−40.3
DO ($mg{\cdot}L^{-1}$)	0.17	3.72
Salinity ($g{\cdot}L^{-1}$)	280	250
Hydrochemistry		
Ions	ppm	
CO_3^{2-}	<6	540 ± 41
HCO_3^-	4545 ± 341	1552 ± 116
Cl^-	101,940 ± 10,194	58,781 ± 5878
Br	264 ± 26	182 ± 18
NO_3^-	<1000	<500
SO_4^{2-}	68,106 ± 6811	78,410 ± 7841
Na^+	59,159 ± 5916	38,507 ± 3851
K^+	6888 ± 689	4488 ± 449
Mg^{2+}	29,755 ± 2976	32,514 ± 3251
Ca^{2+}	144 ± 14	141 ± 14
Si	1.2 ± 0.3	1.7 ± 0.4

Hydrogeochemical modeling of brines						
Mineral	Saturation indices					
	Max	Min	Avg	Max	Min	Avg
Calcite	**2.3**	**0.6**	**1.2**	**2.6**	−1.2	**0.7**
Dolomite	**5.5**	**4.1**	**4.7**	**5.0**	**0.4**	**4.5**
Gypsum	**2.2**	−0.4	−0.1	**2.7**	−0.3	−0.3
Glauberite	**2.0**	−0.6	**0.1**	**3.4**	−0.8	0.1
Bloedite	−1.0	−0.5	−1.5	−0.3	−1.2	−0.5
Epsomite	−0.6	−1.0	−0.6	−0.6	−0.9	−0.6
Hexahydrite	−0.7	−1.1	−0.7	−0.7	−1.1	−0.8
Thenardite	−0.4	−0.8	−0.7	**0.1**	−0.9	−0.3
Mirabilite	−0.5	−1.0	−0.8	**0.2**	−0.9	−0.7
Halite	−0.3	−2.8	−0.9	−0.3	−4.1	−1.0

Bruker D8 Advance diffractometer with Cu Kα radiation (λ = 1.54060 Å). The lithifying microbial mat samples were scanned from 2 to 65° 2θ with a step size of 0.02° 2θ and a counting time of 0.5 s per step. Whereas non-purified EPS samples were scanned under the same conditions, except for a 3 s counting time per step (Fig. 9). XRD interpretation was based on the method described by Chung (1974) using EVA Bruker software. XRD patterns used for specific mineral identification were epsomite (01-072-0696), hexahydrite (00-024-0719) and dolomite (01-074-1687). For mineralogical analysis of clays, approximately around 1 g from each part of the mat were treated as done in Del Buey et al. (2018) with minor modifications. In the same line, ˂2 μm and ˂0.5 μm fractions of the treated sediment were separated using the centrifuge technique. Three XRD diagrams were obtained for each size fraction: after air-drying (AD), ethylene-glycol (EG) and heating at 550 °C for at least 2 h. These samples were scanned from 2 to 35° 2θ with a step size of 0.02° 2θ and a counting time of 1 s per step. The quantification of the clay mineral assemblages was carried out using the mineral intensity factor method (MIF).

2.6. Microelectrode measurements of depth profiles

The concentration of oxygen and sulfide were measured using needle-type microelectrodes. Clark-type potentiometric oxygen and amperometric sulfide electrodes with built-in guard and reference electrodes were connected to a portable model PA 2000 picoammeter (Unisense, Aarhus, Denmark). The sensors were deployed in 100–200 μm depth increments using a manual micromanipulator (National Aperture, New Hampshire). Two to four replicate profiles (i.e. with a horizontal distance of 1–2 mm between individual measurements) covering the upper 10–12 mm of the sediment were measured and the profiles were plotted using calibration curves determined before and after the measurements. Profiles were done in a transect from the decaying submerged mats zone, inside the lake water, to the emerged shore with three distinctive fringing microbial mat zones (Fig. 1c). Two of the three fringing zones were chosen for micro-profiling as the white marginal fringe was dry and thus disregarded. The profiles resulting from the three remaining zones were measured during peak photosynthesis in the middle of the day (the intensity of photosynthetically active radiation (PAR; 400–700 nm) ranged from 1852 to 2178 $\mu E.m^{-2}.s^{-1}$). Oxygen electrodes were checked for the air saturation (100%) signal before each measurement.

During the measurements in each zone, the salinity remained constant and the temperature and PAR fluctuated less than 10%. PAR was measured using a LI-COR LI 250A light meter with a LI-COR LI 190 quantum sensor (LICOR Biosciences, Lincoln, NE, USA).

2.7. Depth distribution of sulfate-reducing activity

The sulfate reduction activity in lithifying microbial mats was mapped immediately upon return to the laboratory. Measurements were done by placing a strip of $^{35}SO_4^{2-}$ coated Ag foil on a freshly cut vertical profile cut of a sediment sample. After 4–6 h incubation at room temperature, the foil was removed, the remaining $^{35}SO_4^{2-}$ washed off and the $^{35}S^{2-}$ that had precipitated as Ag ^{35}S was mapped measured on a BioRad Molecular Imager System GS- 525. The resulting pixel map showed the 2D activity of sulfate reduction in the mat (for details, see Visscher et al., 2000).

2.8. Molecular diversity

2.8.1. DNA extraction, library preparation and sequencing

The DNA was extracted from 0.05 to 0.2 g of the upper and lower mat subsamples using the Power Biofilm DNA Isolation Kit (MO BIO Laboratories, Qiagen, Germantown, MD) following the protocol of the manufacturer. Total DNA in each sample was quantified with a Qubit 2.0 fluorometer (Life Technologies, Carlsbad, CA). Samples were stored at −20 °C until further processed.

The sequences were prepared following the Illumina "16S rRNA genes sequencing library protocol (Illumina, San Diego, CA, USA)". The hypervariable V3-V4 regions of the bacterial and archaeal 16S rRNA gene were amplified using primers that contain 341F and 805R sequences and Illumina-specific adaptors. In a second amplification, Illumina-sequencing adapters and dual-index barcodes was added to the amplicons (Fig. S1). Libraries were quantified with the NEB Next Library Quantification kit and pooled equally. DNA libraries were paired-end sequenced (2 × 300) on an Illumina MiSeq system with the use of the 600 cycle MiSeq Reagent Kit v3 and the protocol recommended by the manufacturer.

DNA extraction, library preparation and sequencing were performed at the Genomics Unit of Complutense University of Madrid.

2.8.2. Analysis of 16S rRNA sequencing data

Sequences were demultiplexed and Illumina adaptors were trimmed with the MiSeq Control software. For taxonomy classification, the obtained FASTQ files of the V3-V4 16S rRNA hypervariable regions were merged, quality filtered, and length trimmed within the CLC Genomics Workbench - Microbial Genomics Module (QIAGEN). Therefore, default parameters were used for merging, filtering and trimming. Operational Taxonomic Units (OTU) clustering was performed considering a 97% of similarity or higher homology between sequences. Subsequently, a representative sequence for each OTU was queried against the Green-Genes database v13.5.

2.9. EPS extraction and purification

The EPS from two lithifying microbial mat samples were further studied in detail. One mat sample was obtained from the transitional fringe (TFZ, Fig. 1d) and the other was taken from the submerged zone (DSZ, Fig. 1e). The samples were mixed with deionized water (1,1 v/v water and EPS) and filtered using 45 μm nitrocellulose. The filtrate was centrifuged in an Eppendorf 5810 R centrifuge for 10 min at 2500 RPM and 4 °C. The supernatant was precipitated using three volumes of ice-cold ethanol (96%) per volume of filtrate during 24 h at 4 °C. The precipitate was recovered by centrifugation (6000 RPM for 10 min) and freeze-dried during 24 h in Telstar Cryodos device.

From 400 g of microbial mats mass, the EPS was recovered and then purified by dialysis. For this last step, out of total amount of EPS, 5 g of freeze-dried powdered EPS was dissolved in 40 ml deionized water by adding 1 ml of 1 M HCl, in order to remove the carbonates and other soluble minerals, while stirring gently. The rehydrated material was placed into a dialysis bag (10 kDa), and dialyzed three times against 1 mM of EDTA for 24 h each time in a cold room at 4 °C. For the final dialysis step, deionized water (>18 MΩ) was used, repeated four times for 24 h. Prior to ITC subsamples were dialyzed one more time against the isothermal titration calorimetry buffer (see below).

2.10. EPS characterization

2.10.1. Acid-base titration

An acid-base titration was used to determine the quantity of proton-binding sites of EPS as well as the potential types and densities of the functional groups. For this titration, 10 ml of the dialyzed EPS was dissolved in 5 ml of de-ionized water to obtain a final volume of 15 ml. Subsequently, 150 μl of 1 M KCl was added. The solution was titrated under N_2 atmosphere to avoid the formation of carbonate ions due to dissolution of atmospheric CO_2 into the EPS solution. The initial pH of the solution was adjusted to 2.4, which required approximately 100 μl of 1 M HCl, and subsequently, the solution was titrated with 0.1 M NaOH added stepwise in 100 μl increments. The pH was recorded until pH 10 was reached using a Hanna pH 211 Microprocessor pH Meter. The titration curves obtained were analyzed using the PROTOFIT 2.1 software. Two standard titration analyses were made with xanthan (0.25% w/v) and dextran sulfate (0.25% w/v) in order to provide a comparison with the natural EPS samples.

2.10.2. Isothermal titration calorimetry (ITC)

Cation-binding properties of natural EPS were investigated using isothermal titration calorimetry (ITC). The enthalpy of cation adsorption to EPS was measured in a TAM III calorimeter (TA instruments) equipped with a micro-reaction system with a 3-ml stainless steel vial. The vial was filled with the sample and lowered into the calorimeter using the manufacturer recommended four-step thermal equilibration procedure. In this assay, the sample was dialyzed against Tris-buffer 30 mM and the ligand was prepared in Tris-buffer 30 mM as described before (Astasov-Frauenhoffer et al., 2017). For the titration, 17–18 injections of 15 μl of 20 mM calcium or magnesium were used with an interval of 45 min between injections. At the end of titration, the data were analyzed using the TAM assistant software (TA instruments, Delaware, USA).

2.10.3. Infrared spectroscopy (ATR-FTIR and FTIR)

The presence of specific functional groups within the EPS such as carboxyl, sulfate/sulfonate/sulfinic, hydroxyl, and amino-groups (Braissant et al., 2007, 2009) was investigated using FT-IR spectroscopic analyses that were conducted both on freeze-dried dialyzed and non-dialyzed samples on a Nicolet Magna 750 FT-IR spectrometer equipped with attenuated total reflectance horizontal accessory (Spectra-Tech H-ATR) fitted with a multibounce ZnSe crystal. Additionally, non-dialyzed EPS samples were prepared using the KBr pellet technique. For this, 2 mg of each sample were mixed with 200 mg of dried KBr and subjected to a pressure of 10 ton·cm^{-2} during 10 min. The Fourier transformed infrared spectrometry (FTIR) was recorded in the 4000 to 400 cm^{-1} range on a NICOLET NEXUS 670–680 spectrometer. The raw data were processed using Origin 2017 graph software.

2.10.4. X-ray photoelectron spectroscopy (XPS)

XPS analyses were performed on non-dialyzed, freeze-dried EPS samples to measure the bulk elemental composition of non-dialyzed EPS. The samples were analyzed using a Leybold Multi probe system equipped with X-ray tube with double Mg/Al anode, electron spectrometer vacuum generators, and an ultra-high vacuum chamber (Leybold LSH-10).

2.10.5. Inductively coupled plasma atomic emission spectroscopy (ICP-AES)

ICP-AES was used on dialyzed EPS to determine the elements strongly attached to the polymeric matrix following dialysis. Non-dialyzed, freeze-dried EPS samples were analyzed by this technique to quantify the bulk elemental composition of major elements (i.e., Na^+, Mg^{2+}, S^+, K^+ and Ca^{2+}) and trace elements attached to EPS samples and to evaluate the effect of the dialysis process in the EPS purification. These analyses were carried out on a SPECTRO Arcos.

2.10.6. Volhard method and ion chromatography

Volhard method was applied to the two non-dialyzed EPS samples in order to quantify the amount of Cl^- present. For these analyses, 2 g of each sample were used in order to obtain the results for duplicate. Additionally, a diluted fraction of both EPS samples was analyzed by ion chromatography to determine dissolved Cl^-.

3. Results

3.1. Physicochemistry and hydrogeochemistry

The physicochemical properties of the water overlying the DSZ (i.e., the water column in the lake) has a lower salinity but higher values for the pH, DO and ORP than in those observed in the TFZ pools (Table 1).

The ionic composition of both TFZ and DSZ water indicated that both could be described as Mg^{2+}-SO_4^{2-}-Cl^- type brine (Table 1). The compositions of both brines were within the hydrogeochemical variation ranges presented by Cabestrero and Sanz-Montero (2018) for lake El Longar (Fig. S5). As Ca^{2+} remained constant, a depletion in Mg^{2+} and SO_4^{2-} and enrichment in monovalent ions (NO_3^-, Cl^-, Na^+ and K^+) was observed when comparing the water column of the lake (DSZ) with that of the pools (TFZ). The mats associated to these pools were well-developed and lithified to a greater degree in comparison to those in DSZ (Fig. 2e). The absence of mineral precipitation within the water column (Fig. 1d–e) indicated either that the lake brine was undersaturated or that spontaneous precipitation did not occur. In the pools, radial aggregates of mirabilite crystallized around gas bubbles and from the margins, where microbial mat surfaces acted as nucleation sites (Fig. S2).

PHREEQC geochemical modeling of the brines confirmed prevalent undersaturation condition for most of sulfates in El Longar (Table 1). Calculations considering average values yielded negative saturation indices (i.e., undersaturation) for sulfate and chloride minerals, with the exception of glauberite, which was slightly supersaturated (SI = 0.1) in both, TFZ and DSZ. In contrast, carbonates were saturated to supersaturated (Table 1). The SI values of the Mg- rich sulfates and chlorides as well as the majority of the Na-sulfates remained negative when considering the analytical errors. Computations using the maximum deviation of ion concentrations substantially increased the degree of saturation of gypsum and glauberite in the two zones (SI ≥ 2), while calculations considering the minimum deviation showed undersaturation of glauberite and locally of calcite (in DSZ).

3.2. Mineralogical characterization

Mineral precipitation in El Longar occur predominantly in the subsurface within the microbial mats, leading to their lithification. The abundance of these intrasedimentary grown crystals decreased from the outer fringes to the submerged zone (Fig. 2a–d). A secondary type of mineral precipitation occurred subaqueously in the small pools that formed across the marginal zone. Complete evaporation of the brine pools caused precipitation of thin films of mirabilite ($Na_2SO_4{\cdot}10H_2O$) around gas bubbles and at the air/brine interface (Fig. S2). This metastable sulfate was readily transformed into the less hydrated mineral thenardite (Na_2SO_4) (Fig. 2e). Subaqueous mineral precipitation within the water column of the lake was not observed (Fig. 1d).

The mineralogy of the lithifying microbial mats consisted of a mixture of sulfates, chlorides, carbonates and silicates (Fig. 2e). The sulfate minerals included gypsum ($CaSO_4{\cdot}2H_2O$), epsomite ($MgSO_4{\cdot}7H_2O$), hexahydrite ($MgSO_4{\cdot}6H_2O$), bloedite ($Na_2Mg(SO_4)_2{\cdot}4H_2O$), mirabilite ($Na_2SO_4{\cdot}10H_2O$), thenardite ($Na_2SO_4$) and glauberite ($Na_2Ca(SO_4)_2$), representing up to 70% of the mineral assemblage (Fig. 2e). These sulfate minerals were packed within the lithifying microbial mats (Fig. 3 and Fig. S3e–h) and frequently coated by subidiomorphic crystals of halite (NaCl), representing up to 5% (Fig. 3b–c). The carbonates, calcite ($CaCO_3$), dolomite (Ca Mg $(CO_3)_2$) and occasional ankerite (Ca (Fe^{2+}, Mg) $(CO_3)_2$), comprised less than 10% of the total mineral fraction (Fig. 2e and Fig. S3c–d). Finally, up to 20% of the sediment consisted of various silicates (quartz, feldspars and phyllosilicates, including a variety of clay minerals; Fig. 2f). Although the bulk mineral composition of the lithifying microbial mats remained quite constant along the transect (Fig. 2e), some differences were observed in the relative abundance of the mineral phases and textures of the lithifying microbial mats. These differences were most evident for gypsum, which was the most abundant mineral. These gypsum crystals were more prevalent in the cyanobacterial lamina (Fig. 3b and Fig. S3a–b) that, in turn, were surrounded by hexahydrite crystals and subidiomorphic aggregates of bloedite growing within the decaying matrix (Fig. 3b–c). The relative abundance of gypsum decreased compared to the Mg, Na-rich sulfates found in the more mature and dehydrated mats lying in the subaerially exposed zones (Fig. 2e). The scattered distribution of bloedite in the microbialites could be due to the fact that this mineral crystallizes preferentially around the voids created by gas (Fig. 2a–b) that were found in the sulfidic layer of the mats (Fig. 4).

The clay mineral assemblage (Fig. 2f) consisted of: illite, kaolinite, chlorite, pyrophyllite, palygorskite, sepiolite and smectite. Del Buey et al. (2018) observed that palygorskite and sepiolite formed in the upper part of microbial mats. Among the newly-formed clay minerals, palygorskite was the most abundant clay mineral in all depth horizons. Sepiolite and smectites contributed a small fraction of the clay assemblage and appeared randomly distributed (Fig. 2f). Palygorskite was observed in voids and typically displayed a curly texture (Fig. 3a).

3.3. Textural and microfabric features of lithifying microbial mats

Microscopic examination of lithifying microbial mats revealed repetitive wavy, laminated patterns formed presumably by filamentous cyanobacteria resulting in microfabrics with vaguely recognizable organic laminae (Fig. S3a–b). The horizontal pattern of the layers was occasionally disrupted by gas pockets or burrowing infauna (Fig. 2a–d, Fig. 3 and Fig. 4). Microbial activity profiles reflected that the formation of voids was linked to areas of sulfide production (Fig. 4 and Fig. 5a). Lenticular to tabular gypsum crystals were ubiquitous within all the mineralizing microbial mats (Fig. 2, Fig. 4, Fig. 5 and Fig. S3a–b) and were associated with clays, carbonates (Fig. S3c–d) and chlorides (Fig. 3a–c). Generally, the size of the gypsum crystals decreased with depth as the sulfide concentration increased (Fig. 4). The majority of the mineral precipitates were embedded in an organic-rich, dark brown matrix of the microbial mats (Fig. S3c–d). The highly crystallized mats in the subaerially exposed zones contain more intrasedimentary Mg-, Na-sulfates and less EPS matrix than in the submerged zone. In general, the Mg- and Na-sulfate crystals were randomly oriented and contained many organic matter inclusions (Fig. S3e–f) that makes them hardly distinguishable from the matrix. Gypsum and, less commonly, other sulfate crystals show distinctive growth zones. Their nuclei are irregular and contain organic inclusions, whilst the outer zones of the crystals are limpid and well developed (Fig. S3e–g).

SEM observations confirmed that the mineralized matrix consisted of

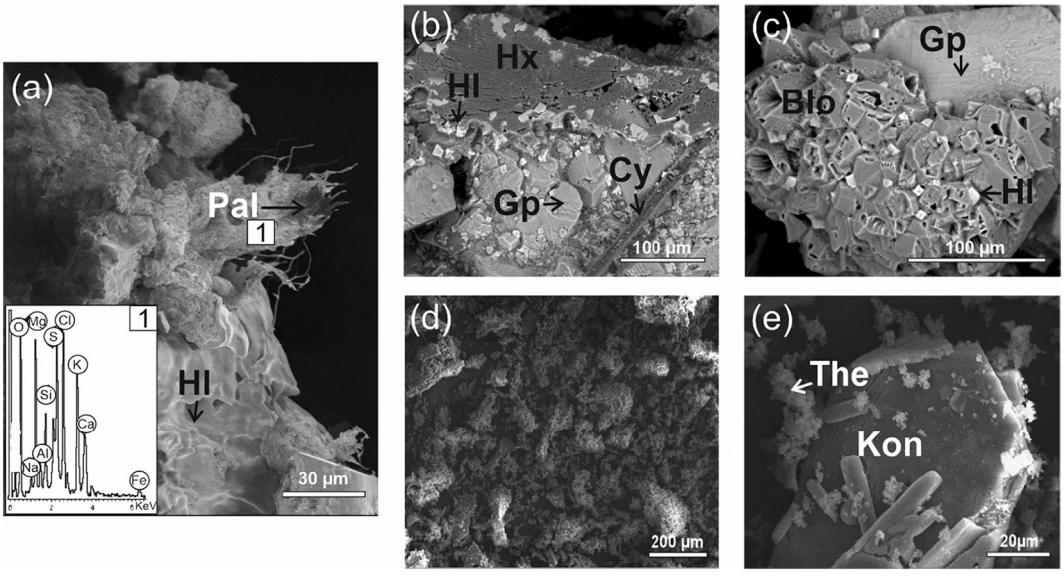

Fig. 3. Scanning electron microphotographs depicting submerged lithifying microbial mat with sulfate minerals (a, b and c) and mineralized EPS formed after freeze-drying (d and e). (a) Curly palygorskite fibers (Pal) in a void of the submerged microbial mats (Fig. 2 d3) associated to sulfates and halite (Hl). The insert in panel (a) shows the spectrum of the Mg-clay. (b) Lenticular gypsum crystals (Gp) covered by hexahydrite (Hx) and halite. A bacterial filament (Cy) is trapped in the sulfates. (c) Aggregates of subidiomorphic bloedite crystals (Blo) coating a gypsum crystal. (d) General view of the clotted texture resulting after freeze-drying of EPS. (e) Idiomorphic konyaite (Kon) crystal covered by microcrystalline thenardite (The) clots.

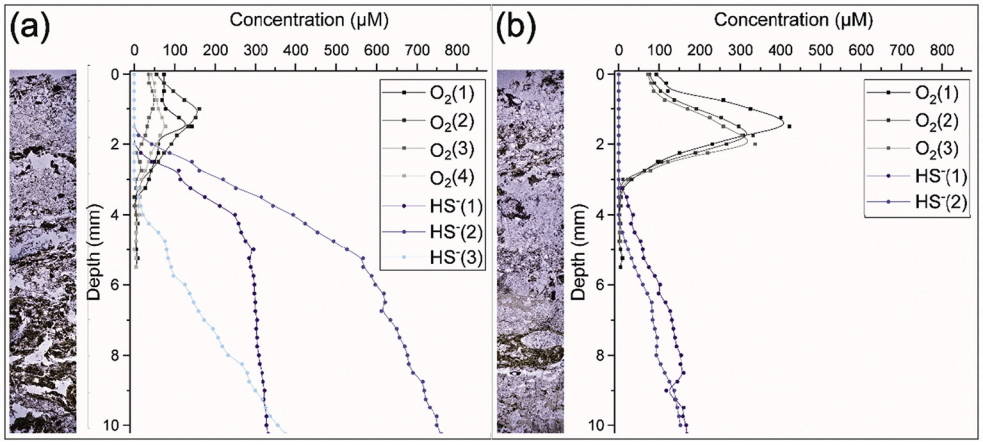

Fig. 4. Thin section microphotographs of the lithifying microbial mats and representative depth profiles of the concentration of O_2 (black circles) and sulfide (blue circles), for the middle fringing zone (MFZ) at the shorelines mats (a) and the decaying submerged mats (DSZ) inside the lake (b). Numbers 1 to 4 represent replicate measurements. HS^- was the dominant (˃80%) sulfide species at the pH measured in the porewater. (For interpretation of the references to colour in this figure legend, the reader is referred to the web version of this article.)

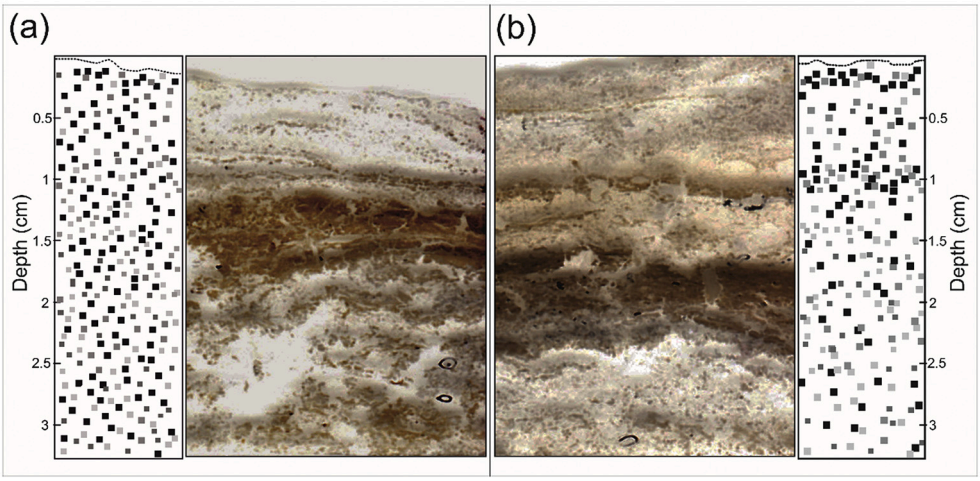

Fig. 5. Thin section microphotographs of the microbial mats and 2D-distribution maps of sulfate reduction activity for the mats from the transitional fringing zones (TFZ, panel a) and mats from the decaying submerged mats zone (DSZ, panel b).

a chaotic mixture of well to poorly defined crystals of Ca, Mg, Na-sulfates and chlorides with scarce organic remains (Fig. S3h). Microcrystalline carbonates occur together with silicate grains surrounding the sulfates (Fig. S3c–d). The formation of cracks around the crystals favors the differentiation of crystals from the embedding matrix (Fig. S3h). A second type of bloedite, comprised of radially intergrown prismatic crystals, coated the pores created by gases.

3.4. Geochemical depth profiles and distribution of sulfate- reducing activity

Microelectrode profiles of oxygen and sulfide were measured in mats present the three inner zones (Fig. 1c MFZ-TFZ-DSZ). Measurements were taken between 11:40 and 13:40 during peak photosynthesis, when the air temperature ranged from 27 to 30 °C, and water temperature increased gradually from 30 to 37 °C. The light intensity remained fairly constant during measurements between 1852 and 2178 μE m^{-2} s^{-1}. Profiles are shown in Fig. 4, for the MFZ (Fig. 4a) and DSZ (Fig. 4b).

Oxygen profiles in both MFZ and DSZ mats showed a characteristic peak at the subsurface (~1–1.5 mm deep). Duplicate profiles measured a few mm apart indicated fairly consistent O_2 distributions with depth. The O_2 maximum in the DSZ mats (331–423 μM, Fig. 4b) was two to fourfold higher than in the MFZ mats (50–161 μM, Fig. 4a). The maximum depth of O_2 penetration ranged from 2 to 4 mm in MFZ mats and was consistently 3 mm in DSZ mats. No (characteristic) O_2 peak was observed in the TFZ mats (Fig. S4) and the depth of the oxic/anoxic interface was approximately 1.5 mm. In both MFZ and DSZ mats, free sulfide appeared immediately when O_2 was depleted. However, in the MFZ mats, sulfide increased more rapidly and reached concentrations of 349–800 μM at 10 mm depth (Fig. 4a). In contrast, sulfide concentrations in the DSZ mats remained below 167 μM at 10 mm depth (Fig. 4b).

The silver foil deployments showed highly active sulfate reduction activity in the upper 3 mm of both TFZ and DSZ mats, starting immediately below the surface (Fig. 5). The darker pixels represent higher sulfide production and thus their distribution can be directly related to the zones of the highest sulfate-reducing activity. The TFZ (Fig. 5a) showed higher rates with a homogeneous distribution. In contrast, slightly lower rates were found in the DSZ mats but these were associated with clearly-defined horizons at the subsurface (˂0.3 mm depth) and at ca. 1 mm depth (Fig. 5b).

3.5. Microbial diversity

The 16S rRNA-based diversity of the four lithifying mats was dominated by Bacteria, and *Archaea* represented up to 19% of the total diversity (Fig. 2f). Among the *Archaea*, the majority were affiliated with the *Halobacteriales* order (Fig. 6).

The bacterial diversity remained relatively similar at the phylum level along the transect (Fig. 2f). In order of decreasing abundance, the bacterial groups included *Firmicutes* (up to 52%) and *Cyanobacteria*

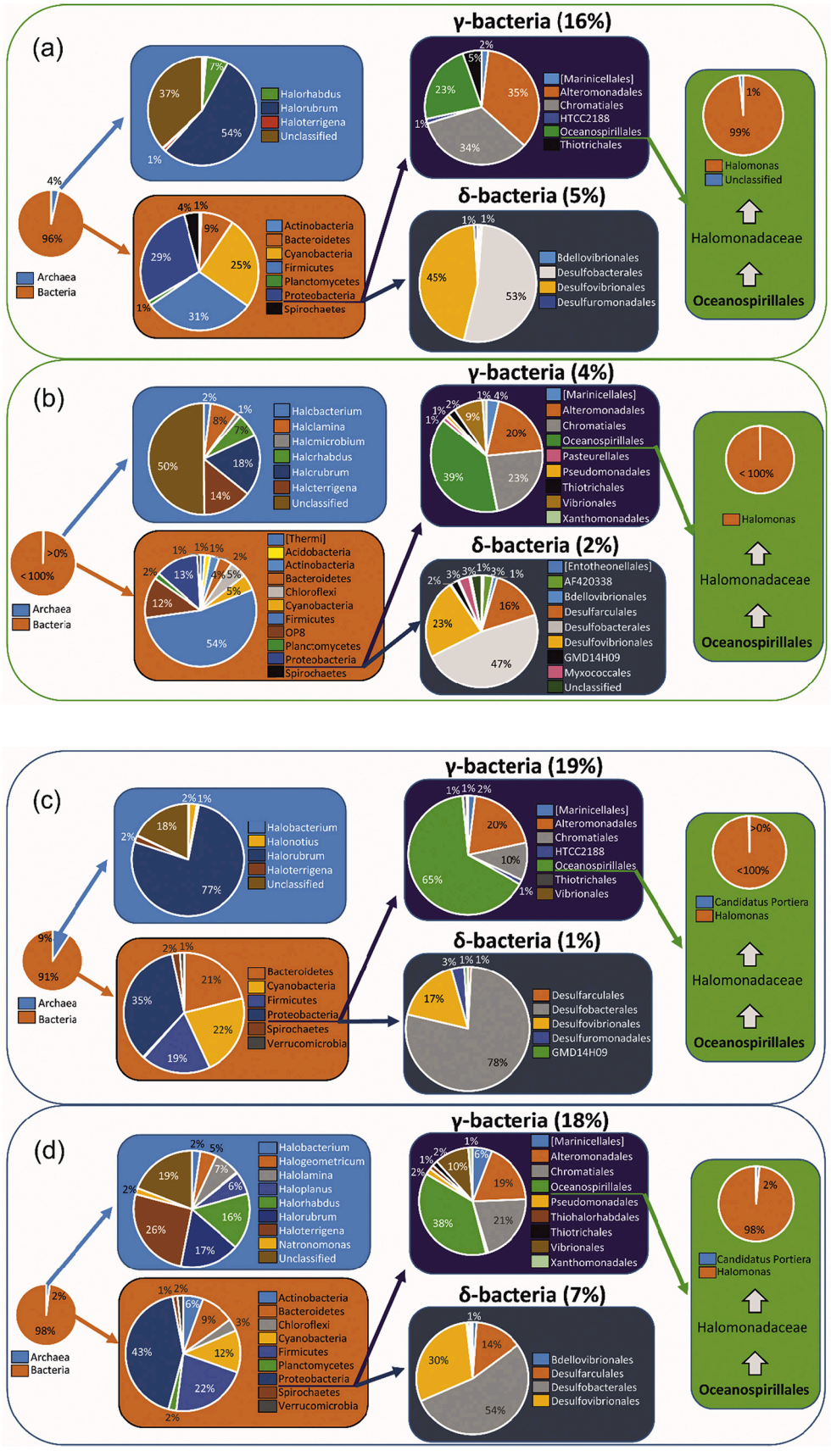

Fig. 6. (a, b, c, d) Pie diagrams of microbial abundance in lithifying microbial mats from pools in the transitional fringing zone (TFZ) (a, upper part and b, lower one) and decaying submerged mats (DSZ) (c, up and d, lower part). The composition of the *δ*- and *γ-Proteobacteria* classes is shown in the dark blue and grey panels (center right) and relative abundance of the *γ-Proteobacterial Halomonas* genus is depicted in the green panel. Note that relative abundances are all given as % of the total prokaryotic diversity.

predominantly represented by the genus *Coleofasciculus* (up to 24%), *Bacteroidetes* (up to 20%), *γ, δ, α Proteobacteria* (up to 22, 22 and 15%, respectively) *and Actinobacteria* (up to 5%). Other phyla with less representation (<5%) were: *Chloroflexi, Spirochaetes, Verrucomicrobia, Planctomycetes,* and *β Proteobacteria* (Fig. 2f and Fig. 6). The phyla *OP8* (11%) and *[Thermi]* (1%) were also detected in the lower horizon of the (TFZ) (Fig. 2c), where the greatest bacterial diversity occurred (Fig. 6b).

The results of bacterial diversity in the four microbial mats revealed a typical microbial stratification at the phylum level (Fig. 2f). Invariably, the number of *Cyanobacteria*, *Bacteroidetes*, *Proteobacteria* (*α* and *γ*) decreased in the lower horizons of all mat types, and the abundance of *Firmicutes* (predominantly, *Clostridia*) increased with depth. *Firmicutes*, were the dominant phylum in the upper mat horizon in the three outer zones (WFZ, MFZ and TFZ), and represented the majority in the lower horizon of the four mats, followed by *δ-Proteobacteria*. An exception to this was found in the lower part of the TFZ mat, which was highly enriched in *Firmicutes* (52%) mainly comprised of *Bacilli* (46%), followed by the phylla *OP8* (11%) and *α Proteobacteria* (5%).

Among the *Proteobacteria*, the classes *δ*- and *γ-Proteobacteria*, which include species involved in sulfur cycling, presented the higher abundances, with the exception of the lower part of TFZ where *α-Proteobacteria* were slightly more abundant (Fig. 2f). Fig. 6 shows the depth distribution of the two groups of *Proteobacteria* at higher taxonomic resolution in TFZ and DSZ mats, revealed that *Desulfobacterales* followed by *Desulfovibrionales* were the dominant orders of *δ-Proteobacteria* (together representing between 75% and 98%; Fig. 6). At the order level, *γ-Proteobacteria* was dominated by *Oceanospirillales* (with the genus *Halomonas* representing >98%), *Chromatiales* and *Alteromonadales* (Fig. 6).

3.6. EPS characterization

ICP-AES and XPS analyses revealed the presence of a variety of elements associated with/in the non-purified EPS of the two analyzed mats (Table 2). These elements remained strongly attached in the purified EPS of the DSZ despite an overall decrease in the amount following dialysis (Table 2). This suggests the presence of two pools of elements in the EPS: one was weakly bound, while the other was more tightly attached to the organic matrix (Braissant et al., 2009). Na^+ (11 ppm) was the most abundant cation, followed closely by elemental S and Mg^{2+} (8 and 5.8 ppm, respectively). K^+ (0.94 ppm) was also abundant in the purified EPS. Na^+, Mg^{2+}, K^+ and Ca^{2+}, important cations of the water brines, occur in a greater extent in the two non-purified EPS (Table 2) than in the overlying brines (Table 1). The concentration of the divalent cations (i.e., Ca^{2+} and Mg^{2+}) were higher in the EPS of DSZ (Table 2) than in the EPS of TFZ (Table 2). In contrast, the quantity of monovalent ions (i.e., Cl^-, K^+ and Na^+) was higher in the latter (Table 2). Several less abundant elements (Sr^{2+}, P^{4+}, Al^{3+} and Si^{4+} and heavy metals like Cr, Mo and Pb) were also present (Table 2), albeit in trace amounts. S $^{6+}$, Cl^-, Si^{4+}, Al^{3+}, Mg^{2+} and Na^+ were important in the precipitation of sulfate, clay, carbonate and chloride minerals. XPS revealed the presence of carbon-carbon bonds (Table 2), and additionally, carbon-oxygen bonds possibly combining in C-O-C and O-C=O chains. Nitrogen was detected as -NH_2 (amine group).

Acid-base titration of EPS from El Longar (Table S2) showed increasing in buffering capacity below pH 2.5. This indicates the presence of different amounts of sulfated functional groups, with pK values below 2.5 (Schiewer, 1999). The pK values between 1.0 and 5.0 are characteristic for carboxylic acids. Weak buffering capacities were measured at a pH around 6.4 and at values between 8 and 9.5. These two buffering capacities were attributed to sulfinic/sulfonic acids and to amino groups, respectively (Stumm and Morgan, 1996; Braissant et al., 2007).

Isothermal titration calorimetry (ITC) showed that at alkaline pH, EPS from El Longar could bind calcium and magnesium within a binding affinity (k) that allows the mineral formation of sulfates, carbonates and

Table 2
Elemental composition of non-purified EPS from the pools zone (TFZ) and purified and non-purified EPS from submerged zone of lake El Longar (DSZ) determined by XPS and ICP-AES. C, N and O were only detected by XPS.

El Longar (TFZ) EPS Chemical Composition

ICP-AES		XPS		
	Non purified	Non purified		
Element	ppm	Element	Atomic %	Assigment
Na	190,000 ± 19,000	Na 2 s	5.6	Na KL_1L_1 Auger Na $L_{23}L_{23}$ Auger
K	28,000 ± 2800	K 2p	1.3	K $2p_{3/2}$ K $2p_{1/2}$ KCl
Mg	32,000 ± 3200	Mg 2 s	5.4	Mg KLL Auger Mg oxide
Ca	539 ± 54	–	–	–
Cl	197,833 ± 9892	Cl 2p	3.9	Cl $2p_{3/2}$ $Cl2p_{1/2}$ Metal Chloride
S	80,000 ± 8000	S 2p	5.5	S $2p_{3/2}$ $S2p_{1/2}$ Metal sulfate
Si	123 ± 14	–	–	–
Al	22 ± 2	Al 2p	3	Al $2p_{3/2}$ Al $2p_{1/2}$ Aluminates
Ba	‹3	–	–	– –
B	–	–	–	– –
Cr	–	–	–	– –
C	–	C 1 s	35.2	C-C C-O-C O-C=O
Fe	18 ± 2	–	–	– –
Li	2.6	–	–	– –
Mn	78	–	–	- -
Mo	–	–	–	– –
N	–	N 1 s	1.8	NH_2
O	–	O 1 s	38.3	Adsorbed oxygen/ Organic C-O
P	52 ± 5	–	–	– –
Pb	–	–	–	– –
Sr	54 ± 5	–	–	– –
Ti	‹5	–	–	– –
Zn	10.5	–	–	– –

El Longar (DSZ) EPS Chemical Composition

ICP-AES			XPS		
	Purified	Non purified	Non purified		
Element	ppm	ppm	Element	Atomic %	Assigment
Na	11	120,000 ± 12,000	Na 2 s	5.6	Na KL_1L_1 Auger Na $L_{23}L_{23}$ Auger
K	0.94	19,000 ± 1900	K 2p	1.4	K $2p_{3/2}$ K $2p_{1/2}$ KCl
Mg	5.8	60,000 ± 6000	Mg 2 s	5.1	Mg KLL Auger Mg oxide
Ca	0.29	814 ± 81	–	–	– –
Cl	–	51,403 ± 2570	Cl 2p	3.2	Cl $2p_{3/2}$ $Cl2p_{1/2}$ Metal Chloride
S	8	140,000 ± 1400	S 2p	5.7	S $2p_{3/2}$ $S2p_{1/2}$ Metal sulfate
Si	0.090 ± 0.009	96 ± 10	–	–	– –
Al	0.016	18 ± 2	Al 2p	2.5	Al $2p_{3/2}$ Al $2p_{1/2}$ Aluminates
Ba	0.022	‹3	–	–	– –
B	0.017	18	–	–	– –
Cr	0.016	‹5	–	–	– –
C	–	–	C 1 s	37.8	C-C C-O-C O-C=O
Fe	0.022	24 ± 2	–	–	– –
Li	‹0.005	13	–	–	– –
Mn	–	32	–	–	- -

(*continued on next page*)

Table 2 (*continued*)

El Longar (DSZ) EPS Chemical Composition					
ICP-AES			XPS		
	Purified	Non purified	Non purified		
Element	ppm	ppm	Element	Atomic %	Assigment
Mo	0.025	19	–	–	– –
N	–	–	N 1 s	1.5	NH_2
O	–	–	O 1 s	37.3	Adsorbed oxygen/ Organic C-O
P	1	28 ± 3	–	–	– –
Pb	0.007	˂3	–	–	– –
Sr	0.072	67 ± 7	–	–	– –
Ti	0.009	˂5	–	–	– –
Zn	0.007	14.5	–	–	– –

clays (i.e., binding and exchange of calcium and magnesium – see Table S3). At the pH tested, the binding of calcium and magnesium was thermodynamically favorable (i.e., spontaneous). The binding affinity for calcium was ranged from $4.5{\cdot}10^4$ kJ/mol (TFZ) to $6.8{\cdot}10^4$ kJ/mol (DSZ). In the case of magnesium, the binding affinity varied from $2.0{\cdot}10^4$ kJ/mol (TFZ) to $3.3{\cdot}10^5$ kJ/mol (DSZ).

ATR-FTIR results confirmed the presence of different functional groups comprising the EPS (Fig. 7a), such as R-COOH (1730–1880 cm^{-1}), R-NH_2 (amide group; 1542 cm^{-1}) and S-O//S=O groups (1025–1072 cm^{-1}). Amino groups were recorded in bands combined with those corresponding to OH^- bands (Fig. 7a). Other N-functional groups, lower in abundance, could include R-NO_2 or C=N-R (bands at 1248.20, 1375.96, 1542.29 and 1620.88 cm^{-1}).

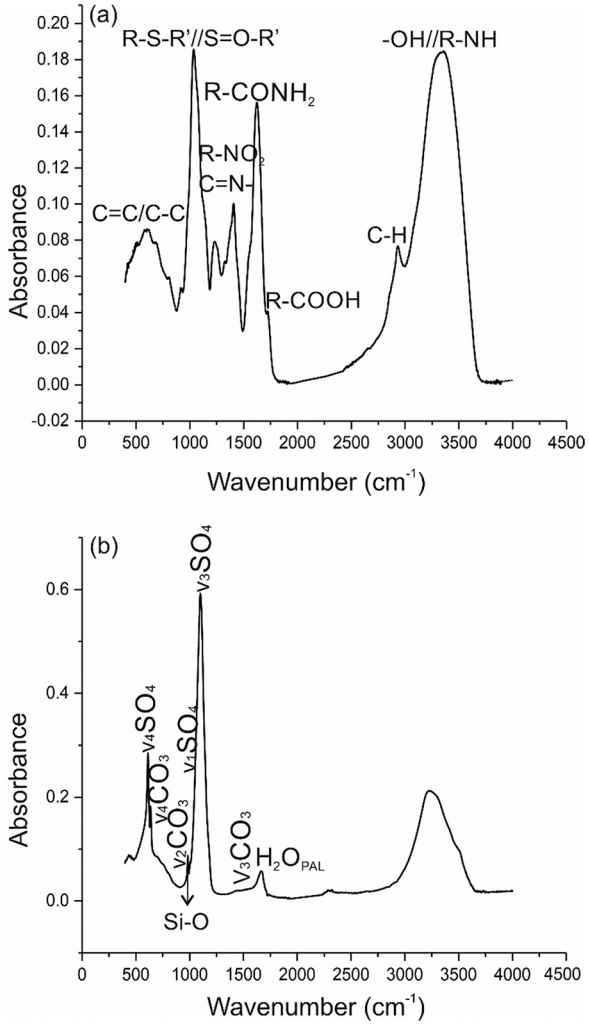

Fig. 7. ATR-FTIR spectra of purified EPS (a) and non-purified EPS from DSZ (b).

When non-dialyzed EPS of TFZ and DSZ were freeze-dried, this caused the precipitation of two distinct groups of well-crystallized minerals as determined by FEI-SEM (Fig. 3d–e), optical and fluorescence microscopy (Fig. 8) and XRD (Fig. 9). These minerals were similar to those that were present in the mats at the sampling date (Fig. 2e). In contrast, the sulfate picromerite ($K_2Mg(SO_4)_2{\cdot}6H_2O$), the molybdenum chloride ($MoCl_2$) and the Fe-hydroxide, bernallite (Fig. 9b) were only synthetic minerals, which were not found in the lake. The association of minerals precipitated from the EPS of DSZ was diverse and mainly comprised of the Mg-sulfate hexahydrite, the double-sulfates konyaite and glauberite, the Na-sulfate thenardite as well as the Mg-clays palygorskite and a talc-like phase (Fig. 9b). Some halite and monohydrocalcite also crystalized from this EPS. The association of minerals formed from the EPS of TFZ was largely made up from bloedite, halite, picromerite and minor glauberite (Fig. 9a). Inspection of these mineral association under a fluorescence microscopy confirmed the transitional gradation of EPS to most of these minerals, commonly forming a continuum phase (Fig. 8). Idiomorphic bloedite and glauberite crystals presented a homogeneous and intense fluorescence (Fig. 8a–f). While prismatic hexahydrite crystals showed a heterogeneous distribution of organic matter inclusions (Fig. 8g–h). Accordingly, the fluorescence intensity varied along the portions of the hexahydrite crystals (Fig. 8i). In the case of halite, most sectors of the crystals were inert (Fig. 8f).

It is important to note that, the Mg-clay palygorskite was only found during the experimental dehydration of EPS from the submerged mats as determined by powder XRD (Fig. 9b) and FTIR results (Fig. S6b). The FTIR results showed the stretching Si—O bond in palygorskite (980 cm^{-1}) and bending modes (1650 cm^{-1}) of absorbed and zeolitic H_2O in palygorskite (Fig. 7b). FTIR analyses based on the KBr method revealed the following peaks (Fig.S6b): the stretching Si—O bonds (1153 cm^{-1}), a smooth shoulder (880 cm^{-1}) related to bending vibration mode of Al-Fe-OH bonds and the fundamental Si-O-Si bond (1186 cm^{-1}) characteristic of palygorskite (Suárez and García-Romero, 2006). Precisely, this vibration (i.e., 1186 cm^{-1}) was the only absent in FTIRspectra of EPS from TFZ (Fig. S6a).

PHREEQC geochemical modeling of ions bound to the EPS from DSZ and TFZ, (Table 3), confirmed that each EPS was supersaturated with respect to the minerals that precipitated during freezing-drying (Fig. 9). In addition, gypsum and thenardite were supersaturated in the EPS from DSZ and TFZ (Table 3), respectively, but did not crystallized during freezing drying (Fig. 9).

4. Discussion

An assemblage of sulfate and carbonate minerals with fibrous clays are found in the rock record of ancient hypersaline lakes (Calvo et al., 1999) that possibly comprised microbial mats (Sanz-Montero and Rodríguez-Aranda, 2012). However, this mineral association is rare in modern lakes and the formation is not well understood. The current study demonstrated that the benthic microbial community in a modern lake, El Longar, controlled the concomitant intrasedimentary precipitation of a variety of hydrated and anhydrous sulfates and fibrous clays. This biogenic control on sediment mineralogy is based on EPS properties, microbial diversity and activity that jointly govern the simultaneous mineral precipitation.

Sulfate minerals dominate the mineral assemblages in the sediments of El Longar (Fig. 2e). These minerals are commonly found in brines of Mg^{2+}-(Na^+) -(Ca^{2+})-SO_4^{2-}(Cl^-) type (Cabestrero and Sanz-Montero, 2018; Cabestrero et al., 2018a). The scarcity and low variability of sulfates precipitated subaqueously from the complete evaporation of

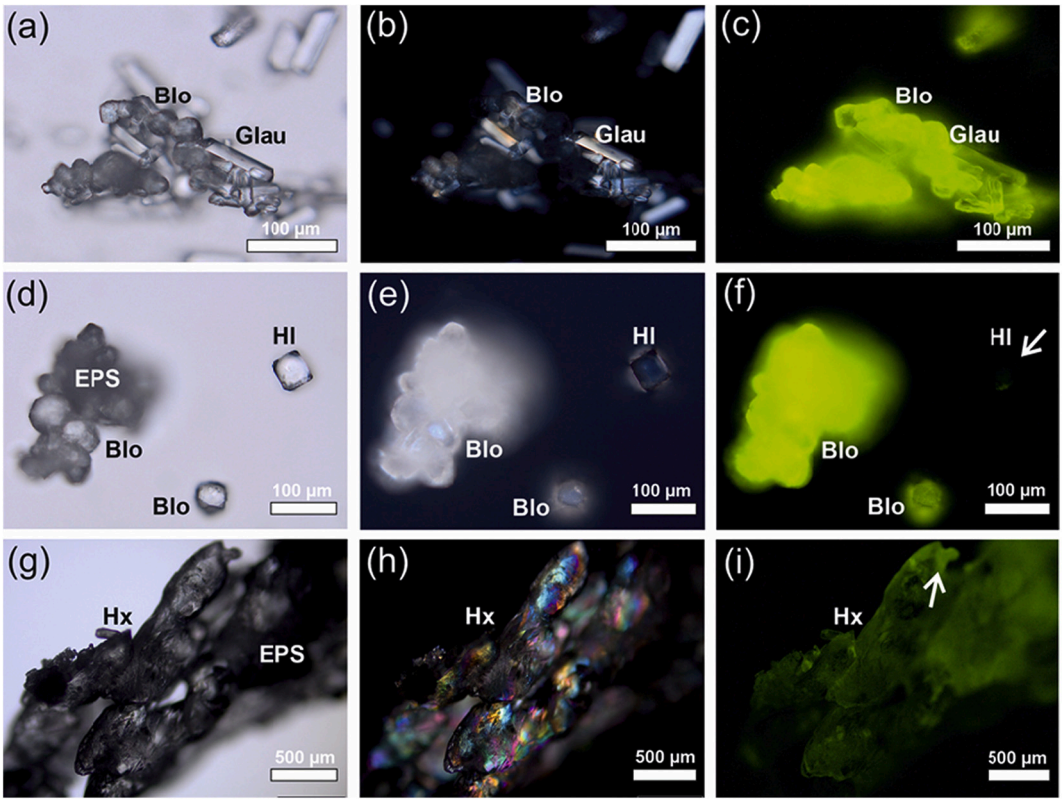

Fig. 8. Microphotographs of minerals precipitated from non-purified EPS. The same fields were viewed under parallel nicols (a, d and g), crossed nicols (b, e and h) and fluorescent light (c, f and i). a–c) Aggregates of tabular glauberite (Glau) and bloedite (Blo) crystals are strongly fluorescent. d-f) A non-fluorescent halite cube (Hl) in the vicinity of an intimate mixture of bloedite crystals and EPS which fluoresce intensely. g–i) Prismatic crystals of hexahydrite (Hx) show an irregular pattern of fluorescence.

natural brines as well as hydrogeochemical modeling based on in situ ion concentrations (Table 1), indicate undersaturation for the most abundant sulfates (i.e., gypsum, bloedite, epsomite and hexahydrite) and chlorides (i.e., halite). The lack of subaqueous mineral precipitation along with modeling efforts of El Longar's brines observed previously (Cabestrero and Sanz-Montero, 2018; Cabestrero et al., 2018a) support undersaturation states for most sulfates in the natural brines even at high salinities (Table S1). These hydrogeochemical conditions may prevent mineral formation in the water column even at very high evaporation rates. Under these conditions only mirabilite aggregates crystallize on the surfaces of nucleation provided by bubbles and mats developed around the pools of the transitional fringe zone (Fig. S2). In parallel, within the mats and completely embedded by their organic matrix, a complex assemblage of minerals precipitates was formed, which lead to their lithification (Fig. 2e). The EPS matrix of the mats forms the primary location for the mineral complex in El Longar (Fig. 8 and Fig. 9). This suggests that microbes and EPS properties influenced the differential precipitation of the mineral assemblage.

The microbial mats (TFZ and MFZ) reached a well-developed stage during the dry season, likely due to the intense brine evaporation (Cabestrero et al., 2018b). This was confirmed by the metagenomic data and microelectrode profiles, revealing that production of carbon (i.e., active photosynthesis) was past its peak (e.g., lower in TFZ and MFZ mats than in DSZ mats; Fig. 4 and Fig. S4). The presence of active cyanobacteria in the upper parts of the mats (Fig. 2f) was documented by a characteristic subsurface peak of O_2 (Fig. 4). However, this O_2 maximum was much higher in DSZ than in MFZ, and completely absent in TFZ (Fig. S4). Although the depth profile depicts the balance of production (oxygenic photosynthesis) and consumption (aerobic respiration, sulfide oxidation and chemical oxidation) of oxygen (Visscher et al., 1998), the decreasing peak value and steepness, suggests a progressive decline in productivity at low depth of the mats along the transect. Likewise, the higher abundance of functional groups, mainly amino groups, in DSZ than in TFZ, as indicated by acid-base titration (Table S2), points to degrading, less metabolically active mats in the outer zone(s). The dominance of *Firmicutes* in the well-developed mats and presence of other organoheterotrophs such as *Bacteroidetes*, some *α-Proteobacteria* and some *Archaea* (Fig. 2f) supports a potential for polymer degradation in the upper sediment layer (Imhoff, 2001). Furthermore, the low molecular weight organic compounds (i.e., mono-, dimers- and fermentation products) produced during the initial degradation of EPS can serve as electron donors for sulfate-reducing bacteria (i.e., *δ-Proteobacteria*) (Visscher et al., 1999; Megonigal et al., 2004; Braissant et al., 2009; Gallagher et al., 2012). This could explain the continuing high sulfate-reducing activity (Fig. 5a) in spite of lower photosynthetic production.

Depth profiles of sulfide, sulfate-reduction maps, microbial diversity and the abundance of sulfate minerals point at vigorous sulfur cycling in the mats of El Longar (Fig. 2f, Fig. 4, Fig. 5 and Fig. S4). The oxidative part of sulfur cycle is mediated by *γ-Proteobacteria* (including colorless sulfur-oxidizing bacteria and purple sulfur bacteria) and also to some extent by *α-Proteobacteria* (purple non-sulfur bacteria), all of which can use sulfide and intermediate sulfur compounds (Kelly, 1982; Visscher et al., 1991; Visscher et al., 1992; Van Gemerden, 1993). Microbial sulfide oxidation must compete with abiotic processes (Megonigal et al., 2004), but the high affinity of sulfide uptake especially by colorless sulfur bacteria (Kelly, 1982; Visscher et al., 1992) suggests that biotic HS^- oxidation outpaces the chemical reaction with O_2 (Millero, 1986). The steepness of the sulfide profile near the oxic-anoxic interface, notably in the DSZ and MFZ mats is a further indication that biological cycling of reduced sulfur compounds is a dominant process.

$^{35}SO_4^{2-}$ reduction mapped on silver foils showed active sulfate reduction in all of the MFZ, TFZ and DSZ mats. Although, the relative

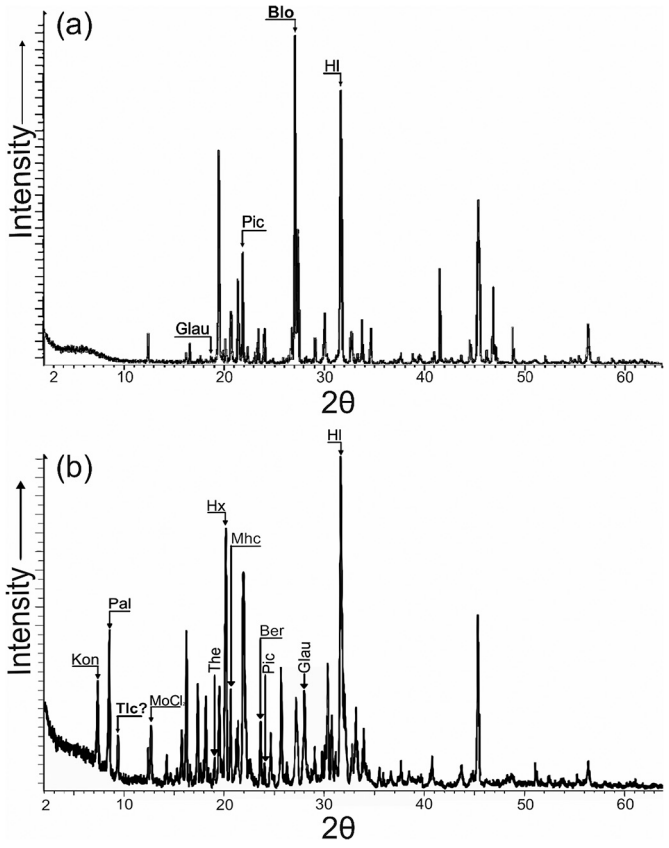

Fig. 9. Powder X-ray diffraction of non-dialyzed natural EPS of the TFZ (a) and DSZ (b). Minerals are bloedite (Blo), picromerite (Pic), glauberite (Glau), halite (Hl), konyaite (Kon), palygorskite (Pal), molybdenum chloride ($MoCl_2$), thenardite (The), hexahydrite (Hx), monohydrocalcite (Mhc), bernallite (Ber), picromerite (Pic), and a talc-like phase (Tlc?).

Table 3
Geochemical modeling results of the maximum, minimum and average saturation indices calculated for sulfates and halite considering ions contained in the non-purified EPS of the transitional fringing zone (TFZ) and decaying submerged zone (DSZ).

Mineral	TFZ			DSZ		
	Saturation indices					
	Max.	Min.	Avg.	Max.	Min.	Avg.
Gypsum	−25.7	−3.6	−9.3	**4.3**	**2**	**2.5**
Glauberite	−10.5	**2**	−0.6	**13.1**	**5.5**	**7.5**
Bloedite	−0.33	**4.3**	**3.5**	**4.6**	**4**	**4.1**
Epsomite	−18.2	−1.9	−6.2	−5.8	**0.3**	−0.8
Hexahydrite	−15.5	−1.3	−5.1	−4.7	**0.5**	−0.4
Thenardite	**8.8**	**3.6**	**5.5**	**5.6**	**2.2**	**3.3**
Mirabilite	−20.11	−3.5	−7.5	−7.2	−1.4	−2.3
Halite	**6.7**	**2.6**	**4**	**2.7**	**0.7**	**1.2**

abundance of *δ-Proteobacteria* was greater at the bottom part of the microbial mats, SRB were also found in the oxic surface layers of the mat, corroborating the observed sulfate reduction activity (Fig. 5). The population of SRB deeper in the mat would benefit from fermentation and partial degradation products of polymers like EPS (Baumgartner et al., 2006; Braissant et al., 2009), and the population near the surface of the mat likely utilized the copious amount of labile organic carbon secreted by the cyanobacteria (Fründ and Cohen, 1992; Visscher et al., 1992). The sulfate-reducing bacteria are not necessarily inhibited by oxygen (Dilling and Cypionka, 1990) and could survive oxic conditions by forming tight consortia with sulfide-oxidizing bacteria (e.g., *γ Proteobacteria*), coordinating their metabolisms (Decho et al., 2010). Similar to our observations in El Longar surface mats, high rates of sulfate reduction were reported in the oxic zone of a variety of microbial mats (Canfield and Des Marais, 1991; Fründ and Cohen, 1992; Visscher et al., 1992, 1998; JØrgensen, 1994; Pace et al., 2016, 2018). Sulfate-reducing bacteria are typically distributed throughout the mat and often show maximum metabolic activity close to the cyanobacteria (Visscher et al., 2000). Additionally, *Halobacteriales* present in the mats (Fig. 6) could contribute, to a lesser extent, to sulfate reduction, even in a wide range of salinities (Elshahed et al., 2004). This active cycling of sulfur may contribute to create locally favorable conditions (i.e., by locally modifying saturation indexes) for the precipitation of undersaturated sulfate minerals as has been shown for carbonate phases (Dupraz and Visscher, 2005). Moreover, EPS properties also promoted the precipitation of this sulfate mineral assemblage (Fig. 9).

Many members of the microbial community may contribute to create the EPS matrix in the microbial mats of El Longar. However, the abundance of cyanobacteria and high rates of photosynthesis mentioned above (Fig. 2f and Fig. 4), suggest that active cyanobacteria are the main producers of EPS, as is common in hypersaline environments (Scheineder et al., 2013). These have the capacity to bind a variety of ions from solution (S^{6+}, Na^{+}, Mg^{2+}, K^{+}, Ca^{2+}, Sr^{2+}, P^{4+}, Si^{4+}, Fe^{2+}, Al^{3+}, among others). Although the concentration of ions bound to the EPS's of the lithifying mats vary along the transect (Table 2), most of ions involved in the precipitation of sulfates and Mg -clay minerals are more concentrated in the EPS matrix than in the natural brines (Table 1 and Table 2). For instance, the concentration of Ca^{2+}, Mg^{2+} and Na^{+} in EPS from DSZ (Table 2) was 5.7, 2.6 and 3.1 times higher, respectively, than in the overlying water (Table 1). The high binding capacity for Ca^{2+} and Mg^{2+} of this EPS from DSZ (Table S3) may prevent the subaqueous mineral precipitation (Figs. 1 d–e and Fig. S2a) by lowering the saturation state (Table 1), as was reported for carbonate minerals in hypersaline mats (Glunk et al., 2009). Likewise, PHREEQC modeling (Table 3) along with the results of the experimental dehydration of El Longar EPS by freeze-drying (Fig. 9) demonstrate that the concentration of ions in these EPS (Table 2) result in positive saturation indices and precipitation for most of minerals present along the transect at the sampling time (Fig. 2e). In the poorly lithified mats of the submerged zone of El Longar (DSZ), the abundance of a variety of elements bound to the EPS (Table 2) indicate their high potential to precipitate several Ca, Mg and Na-sulfates (Table 3). Even though saturation indices prevailing in the submerged EPS predict the formation of gypsum and bloedite among other sulfates (Table 3), these phases did not precipitate during experimental desiccation of this EPS (Fig. 9b). This was further confirmed by the scarce presence of bloedite in these mats (Figs. 2d–e). Indeed, these results demonstrate that the desiccation process of EPS has the potential to precipitate the more hydrated konyaite ($Na_2Mg(SO_4)_2{\cdot}5H_2O$) as well as other Mg-sulfates (e.g., hexahydrite) (Fig. 9b).

The EPS matrix of the marginal mats (TFZ), depleted in Mg^{2+} and Ca^{2+} and enriched in Na^{+} and K^{+} compared to the EPS of submerged mats (Table 2), show a potential to precipitate Na-bearing sulfates (i.e., mainly bloedite and, to a lesser extent, glauberite) (Table 3, Fig. 8 a–f and Fig. 9a). The distribution of bloedite around the voids (Figs. 2c–e) in the sulfidic layer of the senescent mats (Fig. 5a) indicates that this mineral crystallizes preferentially when the mats are being degraded by bacteria and their EPS experienced a rapid desiccation due to evaporation (Fig. 9a). The relative abundance of intrasedimentary Mg-sulfates and the double sulfates compared to gypsum in the mature mats reinforces this notion. Bacterial degradation and the subsequent release of cations bound to EPS are thought to increase the saturation indexes and enhance mineral nucleation (Dupraz et al., 2009; Cabestrero et al., 2018a). Hydrocarbon and solid organic matter inclusions found in bloedite crystals pointed to this precipitation mechanism (Cabestrero et al., 2018a). Other physicochemical processes including UV irradiation, elevated temperature and ionic changes also cause degradation of EPS (Braissant et al., 2009; Dupraz et al., 2009; Dupraz and Visscher,

2005).

Dialysis during EPS purification confirmed that there was a fraction of loosely bound ions (i.e., easily exchanged with the dialysis medium) and another fraction tightly attached to the EPS (i.e., not exchanged during dialysis) (Table 2), suggesting the presence of two ion "pools" (Braissant et al., 2009). The presence of multiple functional groups for complexation with ions corroborated by FTIR and acid-base titration methods (Fig. 7a, Table S2) could explain the different ionic binding affinities of the two pools. Each functional group has characteristic pK values (Phoenix et al., 2002; Braissant et al., 2007), but carboxylic acid and sulfate functional groups bind divalent cations (e.g., $Mg^{2+}$and Ca^{2+}) under fluctuating pH values typical for lithifying mats (Visscher et al., 1998; Phoenix et al., 2002; Braissant et al., 2007). The presence of a variety of functional groups and diverse ions that could be bound to these, reflects the heterogeneous nature of EPS over small spatial (i.e., nm) scales (Decho, 2000), demonstrating their potential to precipitate the suite of minerals observed in the current investigation.

Binding of the divalent cations (i.e., Mg^{2+} and Ca^{2+}) to the EPS matrices occur spontaneously (i.e., $\Delta G < 0$; Table S3). The efficient binding of both Mg^{2+} and Ca^{2+} may explain the widespread formation of Mg-bearing sulfates and Mg-silicates (Fig. 9) and the potential to precipitate gypsum (Table 3). However, gypsum does not nucleate from these mature EPS (Fig. 9). The ability of hydrated Ca^{2+} to diffuse quicker than Mg^{2+} from degraded EPS to the brine (Verrechia et al., 1995; Dupraz and Visscher, 2005), could increase the Mg/Ca ratios in the EPS, favoring the formation of Mg-rich minerals. The binding of other clay mineral-forming metals to EPS (i.e., Si^{4+}, Fe^{2+} and Al^{3+}), may have involved both different functional groups and binding mechanisms. It is suggested that dissolved silica (i.e., likely in the form of $HSiO_4^{3-}$), poorly concentrated in the brines (Table 1) compared to EPS (Table 2), attaches to positively charged amino groups and/or bind through cationic bridging to preexisting bound metallic cations (Urrutia and Beveridge, 1993; Kawano and Tomita, 2001). Accordingly, the presence of the Si-O-Si vibration band (i.e., 1186 cm^{-1}) only in the EPS from DSZ (Fig. S6b) can be explained by a higher density of amino groups in the later than that of EPS from TFZ (Table S2). The Fe^{2+} and Al^{3+} ions may bind to sulfur (i.e., sulfinic acid) or to carboxyl and hydroxyl groups (Urrutia and Beveridge, 1993; Ferris, 2000). In this line, Gutierrez et al. (2012) reported that the EPS secreted by *Halomonas* have a specific binding capacity for many clay-forming elements such as Ca^{2+}, Si^{4+}, $Fe^{2+,3+}$, Mg^{2+} and Al^{3+}.

Initially, the heterogeneous nucleation on the EPS matrix is controlled in space and time by the distribution of cation binding capacity and saturation state of each mineral in hydrated pockets (Decho, 2000; Dupraz et al., 2009). The result of the dehydration of El Longar EPS demonstrate that the desiccation process by itself has the potential to yield the suite of hydrated and anhydrous Mg-sulfates and Mg-silicates observed in the mats (Fig. 8 and Fig. 9). The subsequent crystal growth can be enhanced by an increase of ionic strength and loss of hydroxyl groups during desiccation of EPS (Dohnlakova et al., 2011). The transitional gradation of the sulfates crystallized from the EPS to the organic matrix (Fig. 8), manifested by similar fluorescence signal of the components, strongly support that the crystallization of sulfates occurs within the EPS. Using TEM-AEM, Del Buey et al. (2018) also showed the existence of a gradual transition between ionic chelation in the EPS and Mg-silicate nucleation within the hypersaline mats of El Longar.

These results confirm the impact of biotic interactions on the intrasedimentary formation of a complex assemblage of saline minerals (Fig. 8, Fig. 9 and Fig. 10), including the double sulfate minerals (e.g., konyaite-bloedite and glauberite) and others that typically have been interpreted as having a purely physicochemical origin (Sánchez-Moral et al., 1998). The continuous dehydration of the EPS could also result in the nucleation and growth of well-ordered palygorskite (Fig. 9b). This precipitation mechanism, which is consistent with the highest occurrence of the Mg-clays at the surface of the mats when exposed to the atmosphere (Fig. 2f), was suggested by Del Buey et al. (2018). Other mechanisms invoked for the microbially induced precipitation of Mg-clays from EPS and cyanobacterial sheaths in the zone of active oxygenic photosynthesis (Burne et al., 2014; Pace et al., 2016; Perri et al., 2017) are not observed in lake El Longar.

5. Conclusions

Hypersaline lake El Longar is productive and metabolically diverse. The microbial sulfur cycle in the microbial mats discussed above affects the availability of a wide variety of sulfur compounds in the pore water of the mats. Sulfate originates from the brine and is concentrated through evaporation. However, the mineral-saturation indices as predicted by geochemical modeling and confirmed by the paucity of subaqueous precipitates is insufficiently to promote precipitation of sulfate mineral complexes from the brines. This points at a combined role of EPS properties and sulfur cycling in the mats, by a tight coupling of reductive and oxidative microbial sulfur metabolisms. The EPS matrix of the microbial mats sequesters a range of ions (S, Si, Al, Mg, Na, Ca, among others), which may be responsible for lowering the saturation states of minerals and inhibiting the subaqueous precipitation of many minerals in the lake. Alternatively, subsequent EPS degradation by microbial and desiccation processes, enhance the release of ions that can participate in the early precipitation of sulfate minerals, Mg-silicates, carbonates and chlorides within the microbial mats. Degradation state of EPS controls

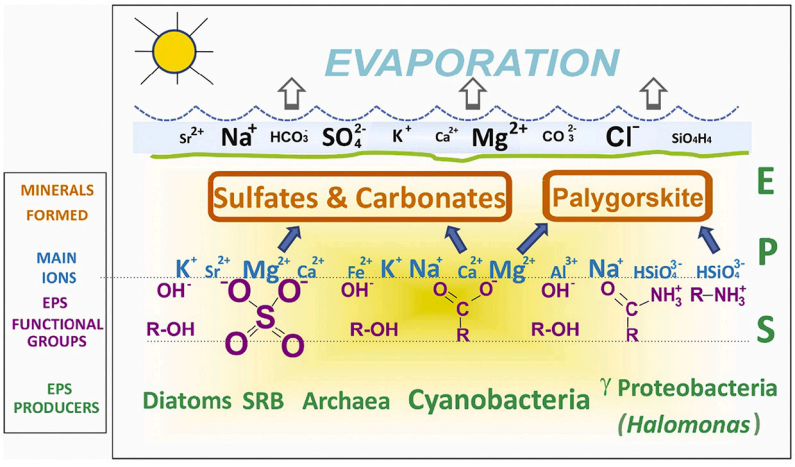

Fig. 10. Mineral formation model of the matured microbial mats in a hypersaline lake subjected to strong evaporation. The EPS produced by several community members bind a great diversity of ions from the surrounding brines.

the type of sulfate mineral (bloedite) and in case of palygorskite, the structural ordering. The density of amino groups in the EPS (matrix) seems to control the growth of the crystal structure of palygorskite through desiccation. Likewise, the formation of a polymineral assemblage through desiccation, implies a critical role for EPS in sulfate and silicate precipitation and ultimately lithification of the microbial mats. At high salinities, the development state of the mat controls its degree of lithification. The implication of our finding is that intrasedimentary sulfate and silicate minerals, that have been present through much of history of the Earth and other celestial bodies, could be of biogenic origin.

Declaration of Competing Interest

The authors declare that they have no known competing financial interests or personal relationships that could have appeared to influence the work reported in this paper.

Acknowledgments

This research work has been funded by the Spanish Ministry of Economy and Competitiveness through National Research Project CGL2015-66455-R (MINECO-FEDER). This project is part of the scientific activities of Research Group UCM-910404. P. Del Buey acknowledges support from a Predoctoral Grant (CT27/16-CT28/16 UCM) and an Internship Grant (EB40/17 UCM) that made him possible to work with Dr. Braissant at Department of Biomedical Engineering, University of Basel (Switzerland). Dr. Visscher acknowledges support from NSF OCE grant 1561173. Dr. Rodríguez-Aranda is acknowledged for his help with the artwork. The authors are grateful to two anonymous reviewers who contributed to the improvement of the manuscript.

Appendix A. Supplementary data

Supplementary data to this article can be found online at https://doi.org/10.1016/j.chemgeo.2021.120403.

References

Astasov-Frauenhoffer, M., Varenganayil, M.M., Decho, A.W., Waltimo, T., Braissant, O., 2017. Exopolysaccharides regulate calcium flow in cariogenic biofilms. PLoS One 12, 1–14.

Awramik, S.M., Buchheim, H.P., 2009. A giant, Late Archaean lake system: the Meentheena member (Tumbiana Formation: Fortescue Group) Western Australia. Precambrian Res. 174, 215–240.

Baumgartner, L.K., Reid, R.P., Dupraz, C., Decho, A.W., Buckley, D.H., Spear, J.R., Przekop, K.M., Visccher, P.T., 2006. Sulfate reducing bacteria in microbial mats: changing paradigms, new discoveries. Sediment. Geol. 185, 131–145.

Bontognali, T.R.R., Martínez-Ruiz, F., McKenzie, J.A., Bahniuk, A., Anjos, S., Vasconcelos, C., 2014. Smectite synthesis at low temperature and neutral pH in the presence of succinic acid. Appl. Clay Sci. 101, 553–557.

Braissant, O., Decho, A.W., Dupraz, C., Glunk, C., Przekop, K.M., Visscher, P.T., 2007. Exopolymeric substances of sulfate-reducing bacteria: interactions with calcium at alkaline pH and implication for formation of carbonate minerals. Geobiology 5, 401–411.

Braissant, O., Decho, A.W., Przekop, K.M., Gallagher, K.L., Glunk, C., Dupraz, C., Visscher, P.T., 2009. Characteristics and turnover of exopolymeric substances in a hypersaline microbial mat. FEMS Microbiol. Ecol. 67, 293–307.

Burne, R.V., Moore, L.S., 1987. Microbialites: organosedimentary deposits of benthic microbial communities. PALAIOS 2, 241–254.

Burne, R.V., Moore, L.S., Christy, A.G., Troitzsch, U., King, P.L., Carnerup, A.M., Hamilton, P.J., 2014. Stevensite in the modern thrombolites of Lake Clifton, Western Australia: a missing link in microbialite mineralization? Geology 42, 575–578.

Cabestrero, Ó., Sanz-Montero, M.E., 2018. Brine evolution in two inland evaporative environments: influence of microbial mats in mineral pecipitation. J. Paleolimnol. 59, 139–157. https://doi.org/10.1007/s10933-016-9908-0.

Cabestrero, Ó., Del Buey, P., Sanz-Montero, M.E., 2018a. Biosedimentary and geochemical constraints on the precipitation of mineral crusts in shallow sulphate lakes. Sediment. Geol. 366, 32–46. https://doi.org/10.1016/j.sedgeo.2018.01.005.

Cabestrero, Ó., Sanz-Montero, M.E., Arregui, L., Serrano, S., Visscher, P.T., 2018b. Seasonal variability of mineral formation in microbial mats subjected to drying and weting cycles in alkaline and hypersaline sedimentary environments. Aquat. Geochem. 24 (1), 79–105. https://doi.org/10.1007/s10498-018-9333-2.

Calvo, J.P., Blanc-Valleron, M.M., Rodríguez-Aranda, J.P., Rouchy, J.M., Sanz, M.E., 1999. Authigenic clay minerals in continental evaporitic environments. In: Simon-Coinçon, M.T.A.R. (Ed.), Palaeoweathering, Palaeosurfaces and Related Continental Deposits. Blackwell Publishing Ldt, pp. 129–151.

Canfield, D.E., Des Marais, D.J., 1991. Aerobic sulfate reduction in microbial mats. Science 251, 1471–1473.

Chung, F.H., 1974. Quantitative interpretation of X-ray diffraction patterns. I. Matrix flushing method for quantitative multicomponent analysis. J. Appl. Crystallogr. 519–931, 7-6D.

Decho, A.W., 1990. Microbial exopolymeric secretions in ocean environments: their role (s) in food webs and marine processes. Annu. Rev. Oceanogr. Mar. Biol. 28, 73–154.

Decho, A.W., 2000. Exopolymer microdomains as a structuring agent for heterogeneity within microbial biofilms. Microbial Sediments. Springer, pp. 9–15.

Decho, A.W., Gutierrez, T., 2017. Microbial extracellular polymeric substances (EPSs) inDesOcean systems. Front. Microbiol. 8, 1–28.

Decho, A.W., Visscher, P.T., Reid, R.P., 2005. Production and cycling of natural microbial exopolymers (EPS) within a marine stromatolite. Palaeogeogr. Palaeoclimatol. Palaeoecol. 219, 71–86.

Decho, A.W., Norman, R.S., Visscher, P.T., 2010. Quorum sensing in natural environments: emerging views from microbial mats. Trends Microbiol. 18, 73–80.

Del Buey, P., Cabestrero, Ó., Arroyo, X., Sanz-Montero, M.E., 2018. Microbially induced palygorskite-sepiolite authigenesis in modern hypersaline lakes (Central Spain). Appl. Clay Sci. 160, 9–21.

Des Marais, D.J., 1995. The biogeochemistry of subtidal marine hypersaline microbial mats, Guerrero Negro, Baja California Sur, Mexico. Adv. Microbial. Ecol. Plenum, New York 251–274.

Dilling, W., Cypionka, H., 1990. Aerobic respiration in sulfate-reducing bacteria. FEMS Microbiol. Lett. 71, 123–128.

Dohnlakova, A.C., Marshall, M.J., Arey, B.W., Williams, K.H., Buck, E.C., Fredrickson, J. K., 2011. Imaging hydrated microbial extracellular polymers: comparative analyses by electron microscopy. Appl. Environ. Microbiol. 77 (4), 1254–1262.

Dupraz, C., Visscher, P.T., 2005. Microbial lithification in marine stromatolites and hypersaline mats. Trends Microbiol. 13, 429–438.

Dupraz, C., Visscher, P.T., Baumgartner, L.K., Reid, P.A., 2004. Microbe-mineral interactions: early carbonate precipitation in a hypersaline lake (Eleuthera Island, Bahamas). Sedimentology 51, 745–765.

Dupraz, C., Reid, R.P., Braissant, O., Decho, A.W., Norman, R.S., Visscher, P.T., 2009. Processes of carbonate precipitation in modern microbial mats. Earth Sci. Rev. 96, 141–162.

Elshahed, M.S., Najar, F.Z., Roe, B.A., Oren, A., Dewwers, T.A., Krumholz, L.R., 2004. Survey of Archaeal Diversity reveals an Abundance of Halophilic Archea in a Low-Salt, Sulfide- and Sulfur-Rich Spring. Appl. Environ. Micobiol. 70, 2230–2239.

Ferris, F.G., 2000. Microbe-metal interactions in sediments. Microbial Sediments. Springer, pp. 121–126.

Fründ, C., Cohen, Y., 1992. Diurnal cycles of sulfate reduction under oxic conditions in cyanobacterial mats. Appl. Environ. Microbiol. 58, 70–77.

Gallagher, K.L., Kading, T.J., Braissant, O., Dupraz, C., Visscher, P.T., 2012. Inside the alkalinity engine: the role of electron donors in the organomineralization potential of sulfate-reducing bacteria. Geobiology 10, 518–530.

Gerdes, G., Klenke, T., Noffke, N., 2000. Microbial signatures in peritidal siliciclastic sediments: a catalogue. Sedimentology 47, 279–308.

Glunk, C., Dupraz, C., Braissant, O., Gallagher, K.L., Verrechia, E.P., Visscher, P.T., 2009. Microbially mediated carbonate precipitation in a hypersaline lake, Big Pond (Eleuthera, Bahamas). Sedimentology 58, 720–736.

Gutierrez, T., Biller, D.V., Shimmield, T., Green, D.H., 2012. Metal binding properties of the EPS produced by Halomonas sp. TG 39 and its potential in enhancing trace element bioavailability to eukaryotic phytoplankton. Biometals 25, 1185–1194.

Imhoff, J.F., 2001. True marine and halophilic anoxygenic phototrophic bacteria. Arch. Microbiol. 176, 243–254.

JØrgensen, B.B., 1994. Sulfate reduction and thiosulfate transformations in a cyanobacterial mat during a diel oxygen cycle. FEMS Microbiol. Ecol. 13, 303–312.

Kawano, M., Tomita, K., 2001. Microbial biomineralization in weathered volcanic ash deposit and formation of biogenic minerals by experimental incubation. Am. Mineral. 86, 400–410.

Kelly, D.P., 1982. Biochemistry of chemiolithotrophic oxidation of inorganic sulphur. Phil. Trans. Roy. Soc. Lond. B 298, 499–528.

Konhauser, K.O., Urrutia, M.M., 1999. Bacterial clay authigenesis: a common biogeochemical process. Chem. Geol. 161, 399–413.

Megonigal, J.P., Hines, M.E., Visscher, P.T., 2004. Anaerobic metabolism: linkages to trace gases and aerobic processes. In: Schlesinger, Willian H., Heinrich, D. Holland, Turekian, Karl K. (Eds.), Treatise on Geochemistry, 8. Elsevier, p. 682. ISBN-0-08-043751-6. 2003, p. 317–424.

Millero, F.J., 1986. The thermodynamics and kinetics of the hydrogen sulfide system in natural waters. Mar. Chem. 18, 121–147.

Pace, A., Bourillot, R., Bouton, A., Vennin, E., Galaup, S., Bundeleva, I., Patrier, P., Dupraz, C., Thomazo, C., Sansjofre, P., Yokoyama, Y., Franceschi, M., Anguy, Y., Pigot, L., Virgone, A., Visscher, P.T., 2016. Microbial and diagenetic steps leading to the mineralization of Great Salt Lake microbialites. Sci. Rep. 6, 31495.

Pace, A., Bourillot, R., Bouton, A., Vennin, E., Braissant, O., Dupraz, C., Duteil, T., Bundeleva, I., Patrier, P., Galaup, S., Yokoyama, Y., Franceschi, M., Virgone, A., Visscher, P.T., 2018. Formation of stromatolite lamina at the interface of oxygenic and anoxygenic photosynthesis. Geobiology 16, 378–398.

Perri, E., Tucker, M.E., Slowakiewicz, M., Whitaker, F., Bowen, L., Perrota, I.D., 2017. Carbonate and silicate biomineralization in a hypersaline microbial mat (Mesaieed sabkha, Qatar): roles of bacteria, extracellular polymeric substances and viruses. Sedimentology 65, 1213–1245.

Phoenix, V.R., Martinez, R.E., Konhaurser, K., Ferris, F.G., 2002. Characterization and implications of the cell surface reactivity of Calothrix sp. strain KC97. Appl. Environ. Microbiol. 68, 4827–4834.
Rossi, F., De Philippis, R., 2015. Role of cyanobacterial exopolysaccharides in phototrophic biofilms and in complex microbial mats. Life 5, 1218–1238.
Rouchy, J.M., Monty, C., 2000. Gypsum microbial sediments: neogene and modern examples. Microbial Sediments. Robert E. Riding and Stanley M. Awramik. pp. 331. ISBN 978-3-662-04036-2. Springer-Verlag Berlin Heidelberg, 2000, p. 209–2016.
Sánchez-Moral, S., Ordóñez, S., García del Cura, M.A., Hoyos, M., Cañaveras, J.C., 1998. Penecontemporaneous diagenesis in continental saline sediments: bleoditization in Quero playa lake (La Mancha, central Spain). Chem. Geol. 149, 189–207.
Sanz-Montero, M.E., Rodríguez-Aranda, J.P., 2012. Magnesite formation by microbial activity: evidence from a Miocene hypersaline lake. Sediment. Geol. 263, 6–15.
Sanz-Montero, M.E., Rodríguez-Aranda, J.P., 2013. The role of microbial mats in the movement of stones on playa lake surfaces. Sediment. Geol. 298, 53–64.
Sanz-Montero, M.E., Rodríguez-Aranda, J.P., García del Cura, M.A., 2008. Dolomite-silica stromatolites in Miocene lacustrine deposits from the Duero Basin, Spain: the role of organotemplates in the precipitation of dolomite. Sedimentology 55, 729–750.
Sanz-Montero, M.E., Calvo, J.P., García del Cura, M.A., Ornosa, C., Outerelo, R., Rodríguez-Aranda, J.P., 2013. The rise of diptera-microbial mat interactions during the Cenozoic: consequences for the sedimentary record of saline lakes. Terra Nova 25, 465–471.
Sanz-Montero, M.E., Cabestrero, Ó., Rodríguez-Aranda, J.P., 2015. Sedimentary effects of flood-producing windstorms in playa-lakes and their role in the movement of large rocks. Earth Surf. Process. Landf. 40, 864–875.
Sanz-Montero, M.E., Cabestrero, Ó., Sánchez-Román, M., 2019. Microbial Mg-rich carbonates in an extreme alkaline lake (Las Eras, Central Spain). Front. Microbiol. 10, 148. https://doi.org/10.3389/fmicb.2019.00148.
Scheineder, D., Arp, G., Reimer, A., Reitner, J., Daniel, R., 2013. Phylogenetic analysis of a microbialite-forming microbial mat from a hypersaline lake of the Kiritimati atoll, Central Pacific. PLoS One 8, 66662, 6 (e).
Schiewer, S., 1999. Modelling complexation and electrostatic attraction in heavy metal biosorption by Sargassum biomass. J. Appl. Phycol. 11, 79–87.
Souza-Egipsy, V., Wierzchos, K., Ascaso, C., Nealson, K.H., 2005. Mg-silica precipitation in fossilization mechanisms of sand tufa endolithic microbial community, Mono Lake (California). Chem. Geol. 217, 77–87.
Spencer, R.D., 2001. In: Alpers, Charles N., Jambor, John L., Nordstrom, D. Kirk, Ribbe, Paul H. (Eds.), Sulfate Minerals in Evaporite Deposits (Chapter 3). Sulfate Minerals: Crystallography, Geochemistry, and Environmental Significance, 40, 2000. Mineral. Soc. Am. Geochem. Soc., p. 608. ISBN 0-939950-52-9.
Stal, L.J., Van Gemerden, H., Krumbein, W.E., 1984. The simultaneous assay of chlorophyll and bacteriochlorophyll in natural microbial communities. J. Microbiol. Meth. 2, 295–306.
Stumm, W., Morgan, J.J., 1996. Aquatic Chemistry. John Wiley & Sons Inc., New York.
Suárez, M., García-Romero, E., 2006. FTIR spectroscopic study of palygorskite: Influence of the composition of the octahedral sheet. Appl. Clay Sci. 31, 154–163.
Sutherland, I.A., 2001. Biofilm exopolysaccharides: a strong and sticky framework. Microbiology 147, 3–9.
Urrutia, M., Beveridge, T., 1993. Mechanism of silicate binding to the bacterial cell wall in Bacillus subtilis. J. Bacteriol. 175, 1936–1945.
Van Gemerden, H., 1993. Microbial mats: a joint venture. Mar. Geol. 113, 3–25.
Verrechia, E.P., Feytet, P., Verrecchia, K.E., Dumont, J.L., 1995. Spherulite in calcrete laminar crusts: biogenic $CaCO_3$ precipitation as a major contributor to crust formation. J. Sediment. Res. 4, 690–700.
Visscher, P.T., Stolz, J.F., 2005. Microbial mats as bioreactors: populations, processes and products. Paleogeogr. Paleoclimatol. Paleoecol. 219, 87–100.
Visscher, P.T., Beukema, J., Van Gemerden, H., 1991. In situ characterization of sediments: measurements of oxygen and sulfide profiles with a novel combined needle electrode. Limnol. Oceanogr. 36, 1476–1480.
Visscher, P.T., Prins, R.A., Van Gemerden, H., 1992. Rates of sulfate reduction and thiosulfate consumption in a marine microbial mat. FEMMS Microbiol. Lett. 86, 283–293.
Visscher, P.T., Reid, R.P., Bebout, B.M., Hoeft, S.E., Macintrye, I.G., Thompson, J.A., 1998. Formation of lithified micritic laminae in modern marine stromatolites (Bahamas): the role of sulfur cycling. Am. Mineral. 83, 1482–1493.
Visscher, P.T., Gritzer, R.F., Leadbetter, E.R., 1999. Low-molecular-weight sulfonates, a major substrate for sulfate reducers in marine microbial mats. Appl. Environ. Microbiol. 65, 3272–3278.
Visscher, P.T., Reid, R.P., Bebout, B.M., 2000. Microscale observations of sulfate reduction: correlation of microbial activity with lithified micritic laminae in modern marine stromatolites. Geology 28, 919–922.